DNS of strong shock and turbulence interactions with thermochemical non-equilibrium effects

Xiaowen Wang* and Xiaolin Zhong #1
Mechanical and Aerospace Engineering Department
University of California, Los Angeles, CA 90095

Abstract

The underlying physics in shock and turbulence interaction is essential for a better understanding of many natural processes as well as scientific and engineering applications, such as volcanic eruption, supernova explosion, detonation, medical application of shock wave lithotripsy to break up kidney stones, and energy application of the implosion of a cryogenic fuel capsule for inertial confinement fusion. One of the fundamental building blocks in these complex processes and applications is the canonical problem of isotropic turbulence and a normal shock. Unfortunately, even this fundamental problem is not well understood for strong shocks. Recent direct numerical simulation (DNS) results of perfect gas flow showed some new trends in turbulent statistics as mean Mach number is increased. In this paper, we first conduct extensive DNS studies on canonical strong shock and turbulence interaction problem of perfect gas flow with mean Mach numbers ranging from 2 to 30. The results show that strong shock waves have a significant effect on turbulent statistics. However, gas temperature increases dramatically after strong shocks so that numerical simulations based on perfect gas flow may not be enough. The effects of thermochemical non-equilibrium flow including internal energy excitations, translation-vibration energy relaxation, and chemical reactions among different species need to be considered. We have developed a new high-order shock-fitting solver for non-equilibrium flow simulations based on the 5-species air chemistry and recently thermal non-equilibrium models. The code package has been tested and is being applied to DNS of strong shock and turbulence interactions with thermochemical non-equilibrium effects.

1. Introduction

The interactions between turbulent flows and shock waves are important in many natural processes as well as scientific and engineering applications, such as volcanic eruption, supernova explosion, detonation, medical application of shock wave lithotripsy to break up kidney stones, and energy application of the implosion of a cryogenic fuel capsule for inertial confinement fusion where very high rates of compression and expansion waves are generally observed. The underlying physics in shock and turbulence interaction is essential for a better understanding of such processes and applications. Unfortunately, these phenomena are strongly nonlinear and proven to be very complex to understand.

One of the fundamental building blocks in these complex processes and applications is the canonical problem of the interaction of isotropic turbulence and a normal shock, and even this fundamental problem is not well understood for strong shocks. Figure 1 shows a schematic of the canonical strong shock and turbulence interaction problem. In such flows, the coupling between shock wave and turbulent flow is very strong. Complex linear and nonlinear mechanisms are involved which alter the dynamics of the shock motion and can cause considerable changes in the structure of turbulence and its statistical properties. This fundamental shock and turbulence

* Research Associate, AIAA Senior Member, E-mail: xiaowen@seas.ucla.edu
# Professor, AIAA Associate Fellow

interaction problem has been a challenge for experimentalists, theorists and computational researchers for more than fifty years.

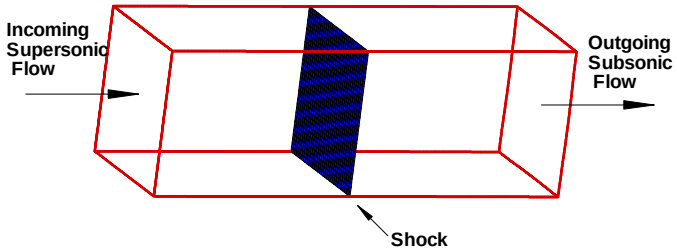

Fig. 1. A schematic of canonical strong shock and turbulence interaction problem [1].

Analytical studies of shock and turbulence interactions have been attempted mostly through linear interaction theory where only small perturbations are considered. Kovasznay [2] showed that, for weak fluctuations of density, pressure, and entropy, turbulent fluctuations about uniform mean flow can be decomposed into acoustic, vorticity, and entropy modes. It was shown that each of these modes evolves independently in the inviscid limit for weak fluctuations. The modifications of random small fluctuations of pressure, entropy and vorticity after passing through shock or flame were studied by Moore [3] and Kerrebrock [4]. It was found that acoustic, vorticity, and entropy modes are generated in the downstream flow if any of the modes is presented in the upstream flow. More recent theoretical studies of shock and turbulence interaction were carried out by Goldstein [5], Lee et al. [6, 7], Mahesh et al. [8, 9] and Fabre et al. [10]. It was found in these studies that the RMS values of fluctuating pressure, temperature, and density as well as different components of turbulent kinetic energy are amplified across the shocks. Despite several assumptions, linear interaction theory satisfactorily predicts the essential characteristics of the interaction of shock waves with freestream turbulence/perturbations, and it is only valid for very small perturbations.

Various attempts have been made towards DNS of shock and turbulence interactions since the early 1980s. Initial efforts were focused on the interaction of shock with simple disturbance waves. In 1981, Pao and Salas [11] fitted the shock at inflow boundary and solved Euler equation with finite difference discretization to study a shock/vortex interaction. Shock-fitting computations with pseudo-spectral (Zang et. al [12]) and spectral techniques (Hussaini et al [13, 14]) were later used to treat the problems in which a single vortex, a vortex sheet, an entropy spot or acoustic wave interacts with the shock. The results obtained from these numerical efforts confirmed the linear theory for weak shocks. With the advent of essentially non-oscillatory (ENO) and related schemes, a number of shock-capturing schemes for compressible flows have been tested for interaction of shock with small disturbances. Although limited to low Mach numbers, these studies mostly confirm the linear interaction analysis results [14-16].

For studies of a fully turbulent flow interacting with shocks, DNS methods and large eddy simulations (LES) have been used. However these different types of methods give different results when interaction with shock is considered [17]. Most of the recent DNS studies have been on various aspects of interaction of a normal shock with freestream turbulence for relatively weak shock at small Mach numbers. For example, Mahesh et al. [8, 9] did extensive DNS studies on the interaction of a normal shock with an isotropic turbulence. The mean shock Mach numbers were in the range of 1.29 to 1.8. They found that the upstream correlation between the vorticity and entropy fluctuations has strong influence on the evolution of the turbulence across the shock. Lee et al. [7] investigated the effect of Mach numbers on isotropic turbulence interacting with a shock wave. The range of Mach numbers was from 1.5 to 3.0. A shock-capturing scheme was

developed to simulate the unsteady interaction of turbulence with shock waves. It was found that turbulence kinetic energy is amplified across the shock wave, and this amplification tends to saturate beyond Mach 3. Hannapel et al. [18] computed shock and turbulence interaction of a Mach 2 shock with a third-order shock-capturing scheme based on the essentially non-oscillatory (ENO) algorithm. Jamme et al. [19] carried out a DNS study of the interaction between normal shock waves of moderate strength (Mach 1.2 and Mach 1.5) and isotropic turbulence. Adams and Shariff [20, 21] proposed a class of upwind-biased finite-difference schemes with a compact stencil for shock and turbulence interaction simulation. They used the non-conservative upwind scheme in smooth region while a shock-capturing ENO scheme was turned on around discontinuities. This idea of hybrid formulation was improved by Pirozzoli [22] who used similar hybrid formulation for a compact weighted essentially non-oscillatory (WENO) scheme with conservative formulation for simulation of shock and turbulence interaction. Ducros et al. [23] conducted LES studies on shock and turbulence interaction by using a second-order finite volume scheme. The method was then used to simulate the interaction of a Mach 1.2 shock with homogeneous turbulence.

It is noticed that flows with stronger than Mach 3 shocks have not been considered in the past for shock and turbulence interaction problems. High-order shock-capturing schemes have been the methods of choice in most previous numerical simulation studies [8, 9, 24, 25]. However, popular shock-capturing schemes are not very accurate in this regard as they inherently use numerical dissipation in the whole computational domain. Moreover, spurious numerical oscillations have been observed when solving strong shock and turbulence interaction problems with shock-capturing schemes [26]. In shock-capturing schemes, the shock generally spreads over a few grid points. With strong shocks, the thickness of the shock front decreases which requires more resolution for shock-capturing schemes. Thus, constraint due to choice of algorithms has been one of the main limitations in past studies. DNS results are currently available for $\mathrm{Re}_\lambda = 12-22$, where Re_λ is Reynolds number based Taylor microscale λ. However, the typical Reynolds number in real shock and turbulence interaction experiments are $\mathrm{Re}_\lambda = 200-750$ [27]. The highest Reynolds number of flow that can be resolved using DNS is bounded by the available computational resources. It was estimated that for DNS of shock and turbulence interaction with $\mathrm{Re}_\lambda \approx 100$ around 19×10^9 grid points were needed [28]. Prohibitively large computational resources are needed for better understanding of realistic flow situations and inadequate computational resources have been another limitation in past studies.

To avoid such problems in existing numerical simulation tools, Rawat and Zhong [1, 29] recently proposed a unique approach of using a high-order shock-fitting and shock-capturing method. The main shock is treated by the shock-fitting method as a sharp boundary of the computational domain. The weak or secondary shocks behind the main shock induced by interactions of the main shock and turbulence are captured by high-order shock-capturing methods. The shock dynamics is governed by a combination of shock jump conditions and a comparability relation from the flow behind main shock. In this way, the interaction of the main shock with freestream turbulence is computed accurately. Compared to shock-capturing methods, the main advantage of the shock-fitting method is uniform high-order accuracy for flow containing shock waves and no spurious oscillations [30]. On the contrary, most of the popular shock-capturing methods are only first-order accurate at the shock and may incur spurious numerical oscillations near the shock. Rawat and Zhong applied the shock-fitting method to DNS studies on strong shock and turbulence interactions of perfect gas flow. The range of shock Mach number is $M = 2-20$. Their results agreed well with those from linear theory and other numerical efforts for weaker than Mach 8 shocks. However, as they increased the shock strengths to the values beyond those

considered in the past, new trends were observed. Specifically, it was found that, in post-shock turbulent flow, the mean value of streamwise velocity is larger than corresponding laminar values whereas the mean value of pressure is smaller than corresponding laminar values (Fig. 2). The difference between turbulent and laminar values decreases as shock strength is increased.

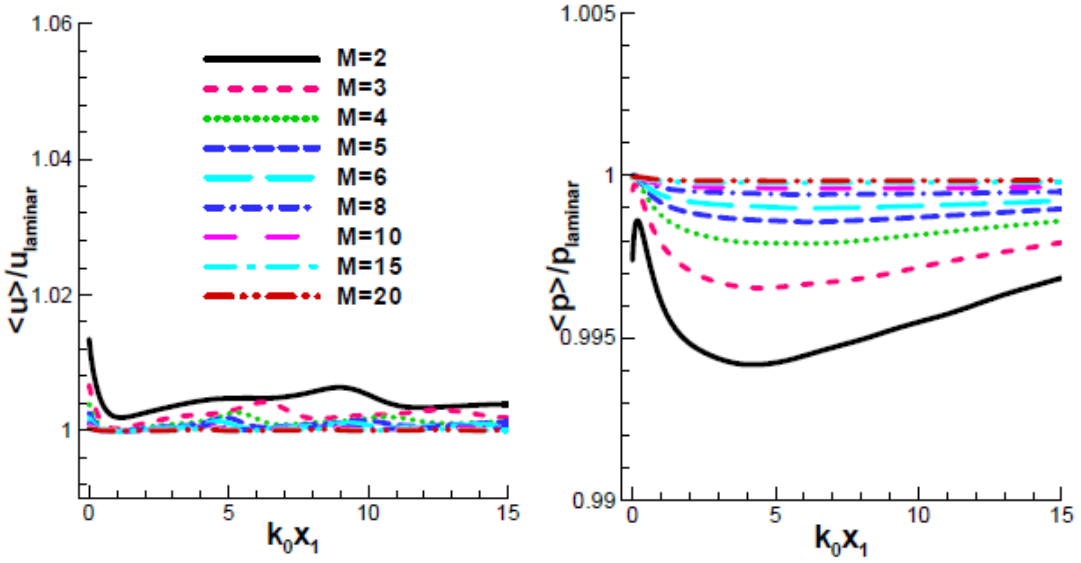

(a) streamwise velocity *(b) pressure*

Fig. 2. Comparison of mean values of flow variables in post-shock turbulent flow with the corresponding laminar values[29].

Figure 3 shows the amplification in streamwise velocity fluctuations for cases with different shock Mach number. It was observed to decrease for weaker than Mach 8 shocks, which is in accordance with the linear theory results. This trend, however, reverses for stronger shocks. Their calculations also showed that, contrary to the previous findings for weaker shocks, increasing shock strength does not simply increase the streamwise vorticity fluctuations. In fact, beyond a certain Mach number, amplification in streamwise vorticity fluctuations decreases and the flow's return to isotropy is delayed (Fig. 4).

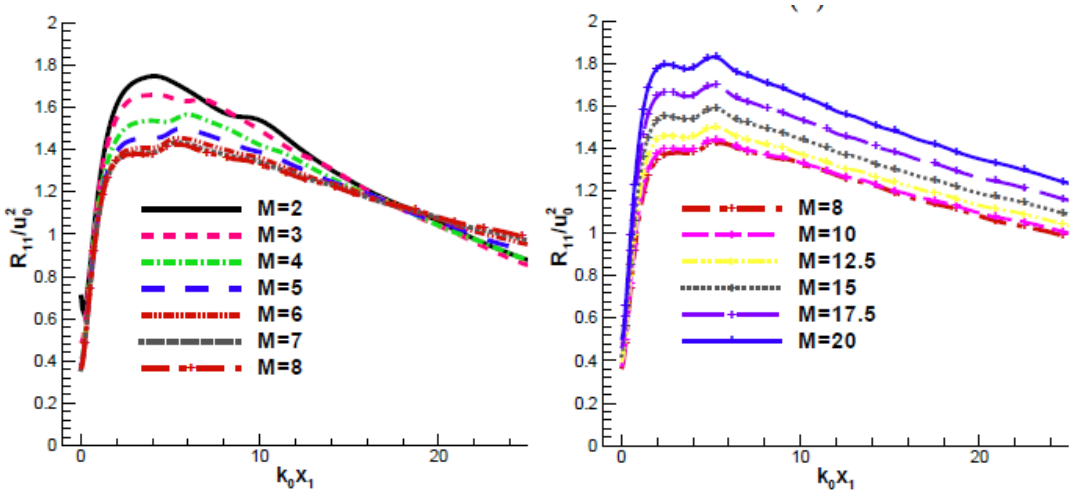

(a) M = 2-8 *(b) M = 8 - 20*

Fig. 3. The amplification in streamwise velocity fluctuations at different shock Mach number [29]

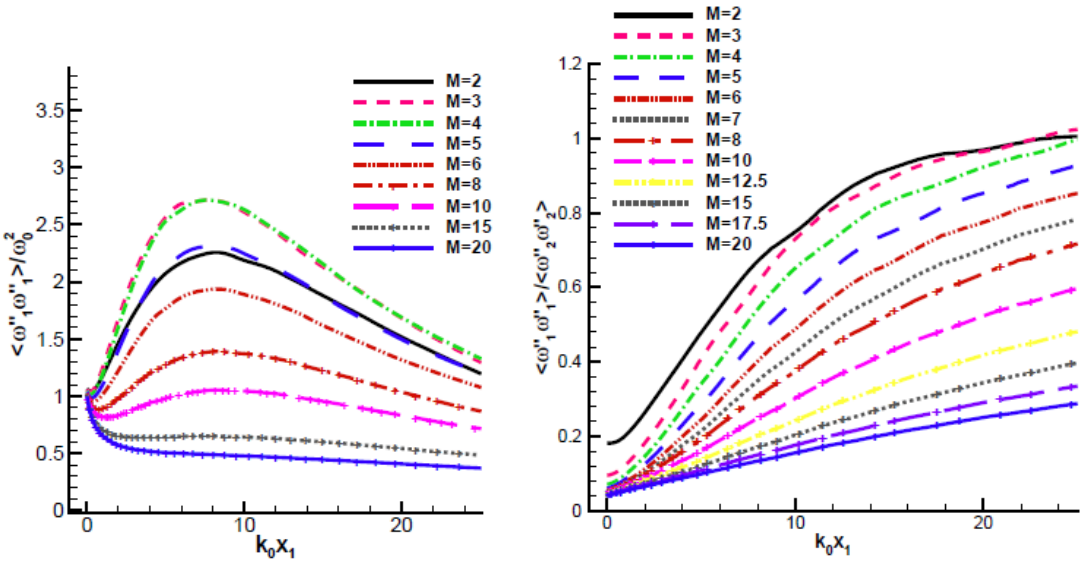

(a) vorticity flucuation *(b) variation of anisotropy*

Fig. 4. Streamwise vorticity fluctuations values for inflow of Re_λ = 29:2 and Mt = 0.124 [29]

The above results are quite interesting and exciting. Basically, for very strong shock, new trends of turbulence statistics appear which is never observed in previous researches for weak shocks.

Literature review of shock and turbulence interactions shows that these complex configurations are part of a number of important applications but the current scientific understanding of strong shock and turbulence interactions in complex configurations and the ability to reliably predict these strongly nonlinear flows remain limited. For turbulent flow interacting with very strong shocks, gas temperature increases dramatically after strong shocks. It is well known that thermal properties of air strongly depend on the temperature [31]. For example, at temperatures above 2000-2500 K, vibration energy mode is fully excited and O_2 starts dissociating. Around 4000 K, O_2 is completely dissociated and N_2 starts dissociating. Therefore, non-equilibrium flow effects including internal energy excitations, translation-vibration energy relaxation, and chemical reactions among different species need to be considered in DNS studies.

The overall objective of this paper is to conduct extensive DNS studies on strong shock and turbulence interactions of perfect gas flow to obtain more quantitative results and to develop and validate a new 3-D high-order shock-fitting code for DNS of non-equilibrium flow. We first conduct extensive DNS studies on canonical strong shock and turbulence interaction problem of perfect gas flow with mean Mach numbers ranging from 2 to 30. The results show that strong shock waves have a significant effect on turbulent statistics. However, gas temperature increases dramatically after strong shocks so that numerical simulations based on perfect gas flow may not be enough. The effects of thermochemical non-equilibrium flow including internal energy excitations, translation-vibration energy relaxation, and chemical reactions among different species need to be considered. We have developed a new high-order shock-fitting solver for non-equilibrium flow simulations based on the 5-species air chemistry and recently thermal non-equilibrium models. The code package has been tested and is being applied to DNS of strong shock and turbulence interactions with thermochemical non-equilibrium effects. The results from non-equilibrium flow simulations will be compared with those from perfect gas flow simulations.

2. Governing equations and numerical methods

2.1 Governing equations of perfect gas flow

The governing equations of perfect gas flow are written in the following conservation-law form in the Cartesian coordinates,

$$\frac{\partial U}{\partial t}+\frac{\partial F_j}{\partial x_j}+\frac{\partial F_{vj}}{\partial x_j}=0 \tag{1}$$

where U, F_j and F_{vj} are the vectors of conservative variables, convective and viscous flux in the direction of jth coordinate, respectively, i.e.,

$$U=\{\rho,\rho u_1,\rho u_2,\rho u_3,e\} \tag{2}$$

$$F_j=\begin{Bmatrix}\rho u_j\\ \rho u_1u_j+P\delta_{1j}\\ \rho u_2u_j+P\delta_{1j}\\ \rho u_3u_j+P\delta_{1j}\\ (e+p)u_j\end{Bmatrix},\ F_{vj}=\begin{Bmatrix}0\\ -\tau_{1j}\\ -\tau_{2j}\\ -\tau_{3j}\\ -\tau_{jk}u_k+q_j\end{Bmatrix} \tag{3}$$

For the simulation of perfect gas flow, the following equations are needed.

$$P=\rho RT \tag{4}$$

$$e=\rho(c_vT+\frac{1}{2}u_ku_k) \tag{5}$$

$$\tau_{ij}=\mu(\frac{\partial u_i}{\partial x_j}+\frac{\partial u_j}{\partial x_i})+\delta_{ij}\lambda\frac{\partial u_k}{\partial x_k} \tag{6}$$

$$q_j=-k\frac{\partial T}{\partial x_j} \tag{7}$$

where R is the gas constant. The specific heat c_v is a constant determined by a given ratio of specific heats γ. The viscosity coefficient μ is calculated by Sutherland's law,

$$\mu=\mu_r\left(\frac{T}{T_0}\right)^{3/2}\frac{T_0+T_s}{T+T_s} \tag{8}$$

For air, $\mu_r=1.7894\times10^{-5}$ Ns/m^2, $T_0=288.0$ K, $T_s=110.33$ K, and $\lambda=-2\mu/3$. The heat conductivity coefficient k is computed by a given Prandtl number.

2.2 Governing equations of thermochemical non-equilibrium flow

The governing equations of thermochemical non-equilibrium flow based on 5-species air chemistry are Navier-Stokes equations with source terms (no radiation). Specifically, they consist of the flowing equations,

$$\frac{\partial\rho_s}{\partial t}+\frac{\partial}{\partial x_j}(\rho_su_j)-\frac{\partial}{\partial x_j}(\rho D_s\frac{\partial y_s}{\partial x_j})=\omega_s \tag{9}$$

$$\frac{\partial}{\partial t}(\rho u_i)+\frac{\partial}{\partial x_j}(\rho u_i u_j+p\delta_{ij})-\frac{\partial}{\partial x_j}\left[\mu\left(\frac{\partial u_i}{\partial x_j}+\frac{\partial u_j}{\partial x_i}\right)-\frac{2}{3}\mu\frac{\partial u_k}{\partial x_k}\delta_{ij}\right]=0 \tag{10}$$

$$\frac{\partial \rho E}{\partial t}+\frac{\partial}{\partial x_j}(\rho H u_j)-\frac{\partial}{\partial x_j}\left[u_i\mu\left(\frac{\partial u_i}{\partial x_j}+\frac{\partial u_j}{\partial x_i}\right)-\frac{2}{3}u_i\mu\frac{\partial u_k}{\partial x_k}\delta_{ij}\right]$$
$$-\frac{\partial}{\partial x_j}\left(\rho\sum_{s=1}^{5}h_s D_s\frac{\partial y_s}{\partial x_j}\right)-\frac{\partial}{\partial x_j}\left(K\frac{\partial T}{\partial x_j}+K_V\frac{\partial T_V}{\partial x_j}\right)=0 \tag{11}$$

$$\frac{\partial \rho E_V}{\partial t}+\frac{\partial}{\partial x_j}(\rho E_V u_j)-\frac{\partial}{\partial x_j}(\rho\sum_{s=1}^{5}e_{V,s}D_s\frac{\partial y_s}{\partial x_j})-\frac{\partial}{\partial x_j}\left(K_V\frac{\partial T_V}{\partial x_j}\right)=\sum_{s=1}^{3}Q_{T-V,s}+\sum_{s=1}^{5}\omega_s e_{V,s} \tag{12}$$

where,

$$\rho=\sum_{s=1}^{5}\rho_s \qquad u_j=\frac{1}{\rho}\sum_{s=1}^{5}\rho_s u_{sj} \qquad y_s=\frac{(\rho_s/M_s)}{\sum_{i=1}^{5}(\rho_i/M_i)}$$

$$p=\sum_{s=1}^{5}p_s=\sum_{s=1}^{5}\frac{\rho_s\bar{R}T}{M_s} \qquad E=\frac{u_i u_i}{2}+\sum_{s=1}^{5}\frac{\rho_s e_s}{\rho} \qquad H=E+\frac{p}{\rho}$$

$\bar{R}$ is the universal gas constant. The formulas of species diffusion coefficient D_s, viscosity μ, heat conductivities K and K_V, species internal energy e_s and $e_{V,s}$, specific vibration energy E_V, and source terms depends on the models of thermochemical non-equilibrium flow.

The corresponding matrix form of governing equations is as follows,

$$\frac{\partial U}{\partial t}+\frac{\partial F_j}{\partial x_j}+\frac{\partial G_j}{\partial x_j}=S \tag{13}$$

where the vector of conservative variables has ten components,

$$U=\left(\rho_1,\rho_2,\ldots,\rho_5,\rho u,\rho v,\rho w,\rho E,\rho e_V\right)^{\mathrm{T}} \tag{14}$$

The inviscid and viscous flux in the direction of jth coordinate, F_j and G_j, and the source term S are given below.

$$F_j=\begin{pmatrix}\rho_1 u_j\\ \rho_2 u_j\\ \vdots\\ \rho_5 u_j\\ \rho u u_j+p\delta_{1j}\\ \rho v u_j+p\delta_{2j}\\ \rho w u_j+p\delta_{3j}\\ \rho H u_j\\ \rho e_V u_j\end{pmatrix},\ G_j=\begin{pmatrix}\rho_1 v_{1j}\\ \rho_2 v_{2j}\\ \vdots\\ \rho_5 v_{5j}\\ -\tau_{1j}\\ -\tau_{2j}\\ -\tau_{3j}\\ -u_i\tau_{ij}+q_j+q_{Vj}+\sum_{s=1}^{5}\rho_s h_s v_{sj}\\ q_{Vj}+\sum_{s=1}^{5}\rho_s e_{V,s}v_{sj}\end{pmatrix},\ S=\begin{pmatrix}\omega_1\\ \omega_2\\ \vdots\\ \omega_5\\ 0\\ 0\\ 0\\ 0\\ \sum_{s=1}^{3}(Q_{T-V,s}+\omega_s e_{V,s})\end{pmatrix} \tag{15}$$

In above equations, $v_{sj} = u_{sj} - u_j$ is diffusion velocity of species s.

$$v_{sj} = -\frac{\rho D_s}{\rho_s}\frac{\partial y_s}{\partial x_j} \tag{16}$$

The model of vibration and electron energy used in Hash et al.'s paper [32] are implemented in the code. Specific total enthalpy of species and specific heat in constant pressure of species are defined as,

$$h_s = c_{vs}T + \frac{p_s}{\rho_s} + e_{V,s} + h_s^0 \tag{17}$$

$$c_p^s = c_v^s + \frac{\overline{R}}{M_s} + c_V^s \tag{18}$$

where h_s^0 is the generation enthalpy of species. The variables on the right hand side of equations (17) and (18) are calculated from the following formula,

$$e_{V,s} = (e_V + e_{els}) = \frac{\overline{R}}{M_s}\left(\sum_{s=1}^{3}\frac{\theta_{vs}}{e^{\theta_{vs}/T_V}-1} + \sum_{s=1}^{5}\frac{\sum_{i=1}^{\infty} g_{i,s}\theta_{el,i,s}\exp(-\theta_{el,i,s}/T_V)}{\sum_{i=0}^{\infty} g_{i,s}\exp(-\theta_{el,i,s}/T_V)}\right) \tag{19}$$

$$c_v^s = c_{vtr,s} + c_{vrot,s} \tag{20}$$

$$c_{vtr,s} = \frac{3\overline{R}}{2M_s},\quad c_{vrot,s} = \begin{cases}\dfrac{\overline{R}}{M_s} & (s = 1,3)\\ 0 & (otherwise)\end{cases} \tag{21}$$

$$c_V^s = \frac{\overline{R}}{M_s}\left\{\frac{(\theta_{vs}/T_V)^2 e^{\theta_{vs}/T_V}}{\left(e^{\theta_{vs}/T_V}-1\right)^2} + \frac{\left[\sum_{i=1}^{\infty} g_{i,s}\left(\theta_{el,i,s}/T_V\right)^2\exp(-\theta_{el,i,s}/T_V)\right]}{\sum_{i=0}^{\infty} g_{i,s}\exp(-\theta_{el,i,s}/T_V)} - \frac{\left[\sum_{i=1}^{\infty} g_{i,s}\theta_{el,i,s}\exp(-\theta_{el,i,s}/T_V)\right]\left[\sum_{i=0}^{\infty} g_{i,s}\left(\theta_{el,i,s}/T_V^2\right)\exp(-\theta_{el,i,s}/T_V)\right]}{\left(\sum_{i=0}^{\infty} g_{i,s}\exp(-\theta_{el,i,s}/T_V)\right)^2}\right\} \tag{22}$$

For the 5-species air, the related parameters used in the models of vibration and electron energy are listed in Table 1 and Table 2. Compared to other models [33, 34], the current models have the advantage of directly applicable to unlimited high temperatures.

Table 1. Parameters used vibration energy model

Species	h_s^0 (J/kg)	M_s (g)	θ_{vs} (K)
N2	0	28	3395
O2	0	32	2239
NO	2.996123e6	30	2817
N	3.362161e7	14	-
O	1.543119e7	16	-

Table 2. Electronic energy states for 5-species air

Species	Θ (K)	g	Species	Θ (K)	g	Species	ΘO (K)	g
N2	0	1	O2	1.13916e4	2	NO	8.88608e4	4
N2	7.22316e4	3	O2	1.89847e4	1	NO	8.98176e4	4
N2	8.57786e4	6	O2	4.75597e4	1	NO	8.98845e4	2
N2	8.60503e4	6	O2	4.99124e4	6	NO	9.04270e4	2
N2	9.53512e4	3	O2	5.09227e4	3	NO	9.06428e4	2
N2	9.80564e4	1	O2	7.18986e4	3	NO	9.11176e4	4
N2	9.96827e4	2	NO	0	4	N	0	4
N2	1.04898e5	2	NO	5.46735e4	8	N	2.76647e4	10
N2	1.11649e5	5	NO	6.31714e4	2	N	4.14931e4	6
N2	1.22584e5	1	NO	6.59945e4	4	O	0	5
N2	1.24886e5	6	NO	6.90612e4	4	O	2.27708e2	3
N2	1.28248e5	6	NO	7.0500e4	4	O	3.26569e2	1
N2	1.33806e5	10	NO	7.49106e4	4	O	2.28303e4	5
N2	1.40430e5	6	NO	7.62888e4	2	O	4.86199e4	1
N2	1.50496e5	6	NO	8.67619e4	4			
O2	0	3	NO	8.71443e4	2			

For the 5-species air, a more complex model of thermal properties is applied [35]. Thermal properties are calculated as follows,

$$\mu = \sum_s \frac{m_s \gamma_s}{\sum_r \gamma_r \Delta_{sr}^{(2)}(T)} \quad \textbf{(g/cm-sec)} \tag{23}$$

$$K_T = \frac{15}{4} k \sum_s \frac{\gamma_s}{\sum_r a_{sr} \gamma_r \Delta_{sr}^{(2)}(T)} \quad \textbf{(J/cm-sec-K)} \tag{24}$$

In above equation, $a_{sr} = 1 + \frac{\left[1-(m_s/m_r)\right]\left[0.45-2.54(m_s/m_r)\right]}{\left[1+(m_s/m_r)\right]^2}$.

$$K_R = k \sum_{s=1,2,3} \frac{\gamma_s}{\sum_r \gamma_r \Delta_{sr}^{(1)}(T)} \quad \textbf{(J/cm-sec-K)} \tag{25}$$

$$K_{V-E} = k \frac{C_{V,V}}{R} \sum_{s=1}^{5} \frac{\gamma_s}{\sum_r \gamma_r \Delta_{sr}^{(1)}(T)} \quad \textbf{(J/cm-sec-K)} \tag{26}$$

To calculate viscosity and heat conductivity, the collision terms are as follows,

$$\Delta_{sr}^{(1)}(T)=\frac{8}{3}\left[\frac{2m_s m_r}{\pi RT(m_s+m_r)}\right]^{1/2}10^{-20}\pi\Omega_{sr}^{(1,1)}(T)\ \textbf{(cm-sec)}$$

$$\Delta_{sr}^{(2)}(T)=\frac{16}{3}\left[\frac{2m_s m_r}{\pi RT(m_s+m_r)}\right]^{1/2}10^{-20}\pi\Omega_{sr}^{(2,2)}(T)\ \textbf{(cm-sec)}$$

Collision integrals involving neutrals (Non-Coulombic collision integrals) are

$$\pi\Omega_{sr}^{(l,j)}(T)=DT^{\left[A(\ln T)^2+B\ln T+C\right]}\ (\overset{0}{\mathrm{A}}^2) \tag{27}$$

Species diffusion coefficients are defined as,

$$D_s=\frac{(1-y_s)}{\sum_{r\neq s}(y_r/D_{sr})} \tag{28}$$

For binary diffusion between heavy particles, $D_{sr}=\dfrac{kT}{p\Delta_{sr}^{(1)}(T)}$. The heat conductivities K and K_V in governing equations are calculated as,

$$K=K_T+K_R \tag{29}$$

$$K_V=K_{V-E} \tag{30}$$

For chemical non-equilibrium, five reactions are considered for the five species air, i.e.,

$$\left.\begin{aligned} N_2+M&=2N+M\\ O_2+M&=2O+M\\ NO+M&=N+O+M\\ N_2+O&=NO+N\\ NO+O&=O_2+N \end{aligned}\right\} \tag{31}$$

Correspondingly, the reaction rates are calculated as follows,

$$\left\{\begin{aligned} R_1&=\sum_m\left[-k_{f_1m}\frac{\rho_{N_2}}{M_{N_2}}\frac{\rho_m}{M_m}+k_{b_1m}\frac{\rho_N}{M_N}\frac{\rho_N}{M_N}\frac{\rho_m}{M_m}\right]\\ R_2&=\sum_m\left[-k_{f_2m}\frac{\rho_{O_2}}{M_{O_2}}\frac{\rho_m}{M_m}+k_{b_2m}\frac{\rho_O}{M_O}\frac{\rho_O}{M_O}\frac{\rho_m}{M_m}\right]\\ R_3&=\sum_m\left[-k_{f_3m}\frac{\rho_{NO}}{M_{NO}}\frac{\rho_m}{M_m}+k_{b_3m}\frac{\rho_N}{M_N}\frac{\rho_O}{M_O}\frac{\rho_m}{M_m}\right]\\ R_4&=-k_{f_4}\frac{\rho_{N_2}}{M_{N_2}}\frac{\rho_O}{M_O}+k_{b_4}\frac{\rho_{NO}}{M_{NO}}\frac{\rho_N}{M_N}\\ R_5&=-k_{f_5}\frac{\rho_{NO}}{M_{NO}}\frac{\rho_O}{M_O}+k_{b_5}\frac{\rho_{O_2}}{M_{O_2}}\frac{\rho_N}{M_N} \end{aligned}\right. \tag{32}$$

Finally, the source terms are as follows,

$$\begin{cases} \omega_{N_2} = M_{N_2}(R_1 + R_4) \\ \omega_{O_2} = M_{O_2}(R_2 - R_5) \\ \omega_{NO} = M_{NO}(R_3 - R_4 + R_5) \\ \omega_N = M_N(-2R_1 - R_3 - R_4 - R_5) \\ \omega_O = M_O(-2R_2 - R_3 + R_4 + R_5) \end{cases} \tag{33}$$

The forward and backward reaction rate coefficients have the form of

$$k_f\left(\overline{T}\right) = C_f \overline{T}^{\eta_f} \exp\left(-\theta_f / \overline{T}\right) \tag{34}$$

$$k_b\left(T\right) = \frac{k_f(T)}{k_{eq}(T)} \tag{35}$$

For dissociation reactions, $\overline{T} = \sqrt{TT_V}$. For the other reactions, the control temperature is $\overline{T} = T$. The equilibrium constant is obtained using the curve fits of Park [36], i.e.,

$$k_{eq} = \exp(a_1 z^{-1} + a_2 + a_3 \ln z + a_4 z + a_5 z^2) \tag{36}$$

In two temperature model, energy relaxation only happens between translation energy and vibration & electron energy, which can be expressed as

$$Q_{T-v,s} = \rho_s \frac{e_{vs}^*(T) - e_{vs}}{\tau_{vs}} \tag{37}$$

where, $e_{vs}^*(T)$ is the vibration energy per unit mass of species s evaluated at the local translational temperature.

$$\tau_{vs} = \left\langle \tau_{s,L-T} \right\rangle + \tau_{cs} = \frac{\sum_r y_r}{\sum_r y_r / \tau_{sr,L-T}} + \frac{1}{a_s \sigma_v N_s} \qquad (a_s = \sqrt{\frac{8\overline{R}T}{\pi M_s}})$$

$$\tau_{sr,L-T} = \frac{1}{p} \exp\left[A_{sr}\left(T^{-1/3} - 0.015\mu_{sr}^{1/4}\right) - 18.42 \right] \text{ (p in atm)}$$

$$A_r = 1.16 \times 10^{-3} \mu_{sr}^{1/2} \theta_{vs}^{4/3} \qquad \mu_{sr} = M_s M_r / (M_s + M_r)$$

$$S_s = 3.5 \exp\left(-\theta_s / T_{shk} \right) \qquad \sigma_v = 10^{-21} \left(50,000 / T \right)^2$$

Here, θ_s is a defined characteristic temperature listed in Table 1.

2.3 Coordinate transform

The flow solver uses structured grids. The following grid transform is applied in the computational domain,

$$\begin{cases} x = x(\xi, \eta, \zeta, \tau) \\ y = y(\xi, \eta, \zeta, \tau) \\ z = z(\xi, \eta, \zeta, \tau) \\ t = \tau \end{cases} \Leftrightarrow \begin{cases} \xi = \xi(x, y, z, t) \\ \eta = \eta(x, y, z, t) \\ \zeta = \zeta(x, y, z, t) \\ \tau = t \end{cases} \tag{38}$$

The Jacobian of the above coordinate transform is,

$$J = \begin{vmatrix} x_\xi & y_\xi & z_\xi & 0 \\ x_\eta & y_\eta & z_\eta & 0 \\ x_\zeta & y_\zeta & z_\zeta & 0 \\ x_\tau & y_\tau & z_\tau & 1 \end{vmatrix} \tag{39}$$

With the transform, the governing equations in (ξ, η, ζ, τ) coordinate system are written as

$$\frac{\partial (JU)}{\partial \tau} + \frac{\partial \tilde{F}_1}{\partial \xi} + \frac{\partial \tilde{F}_2}{\partial \eta} + \frac{\partial \tilde{F}_3}{\partial \zeta} + \frac{\partial \tilde{G}_1}{\partial \xi} + \frac{\partial \tilde{G}_2}{\partial \eta} + \frac{\partial \tilde{G}_3}{\partial \zeta} = JS \tag{40}$$

where

$$\begin{aligned}
\tilde{F}_1 &= J\xi_x F_1 + J\xi_y F_2 + J\xi_z F_3 + JU\xi_t \\
\tilde{F}_2 &= J\eta_x F_1 + J\eta_y F_2 + J\eta_z F_3 + JU\eta_t \\
\tilde{F}_3 &= J\zeta_x F_1 + J\zeta_y F_2 + J\zeta_z F_3 + JU\zeta_t \\
\tilde{G}_1 &= J\xi_x G_1 + J\xi_y G_2 + J\xi_z G_3 \\
\tilde{G}_2 &= J\eta_x G_1 + J\eta_y G_2 + J\eta_z G_3 \\
\tilde{G}_3 &= J\zeta_x G_1 + J\zeta_y G_2 + J\zeta_z G_3
\end{aligned}$$

2.4 Numerical method

The governing equations are solved by the fifth-order shock-fitting method of Zhong [37]. For the thermochemical non-equilibrium system (13) in the direction, $\mathrm{k} = (k_1, k_2, k_3)$, the corresponding inviscid flux term is

$$\mathrm{F} = \begin{pmatrix} \rho_1 \mathrm{k\,u} \\ \rho_2 \mathrm{k\,u} \\ \rho_3 \mathrm{k\,u} \\ \rho_4 \mathrm{k\,u} \\ \rho_5 \mathrm{k\,u} \\ \rho u \mathrm{k\,u} + p k_1 \\ \rho v \mathrm{k\,u} + p k_2 \\ \rho w \mathrm{k\,u} + p k_3 \\ \rho H \mathrm{k\,u} \\ \rho E_V \mathrm{k\,u} \end{pmatrix} \tag{41}$$

Hence the Jacobian of flux is defined as,

$$\mathrm{A} = \frac{\partial \mathrm{F}}{\partial \mathrm{U}} = L \Lambda R \tag{42}$$

$$A=|\mathrm{k}|\begin{bmatrix}\tilde{U}(\delta_{sr}-c_s) & c_s n_x & c_s n_y & c_s n_z & 0 & 0\\ \tilde{\gamma}_r n_x-\tilde{U}u & -\beta u n_x+u n_x+\tilde{U} & -\beta v n_x+u n_y & -\beta w n_x+u n_z & \beta n_x & \phi n_x\\ \tilde{\gamma}_r n_y-\tilde{U}v & -\beta u n_y+v n_x & -\beta v n_y+v n_y+\tilde{U} & -\beta w n_y+v n_z & \beta n_y & \phi n_y\\ \tilde{\gamma}_r n_z-\tilde{U}w & -\beta u n_z+w n_x & -\beta v n_z+w n_y & -\beta w n_z+w n_z+\tilde{U} & \beta n_z & \phi n_z\\ \tilde{\gamma}_r\tilde{U}-\tilde{U}H & -\beta u\tilde{U}+H n_x & -\beta v\tilde{U}+H n_y & -\beta w\tilde{U}+H n_z & \beta\tilde{U}+\tilde{U} & \phi\tilde{U}\\ -\tilde{U}e_V & e_V n_x & e_V n_y & e_V n_z & 0 & \tilde{U}\end{bmatrix}$$

$$R=\begin{bmatrix}a^2\delta_{sr}-c_s\tilde{\gamma}_r & \beta u c_s & \beta v c_s & \beta w c_s & -\beta c_s & -\phi c_s\\ -\tilde{V} & l_x & l_y & l_z & 0 & 0\\ -\tilde{W} & m_x & m_y & m_z & 0 & 0\\ \tilde{\gamma}_r-\tilde{U}a & a n_x-\beta u & a n_y-\beta v & a n_z-\beta w & \beta & \phi\\ \tilde{\gamma}_r+\tilde{U}a & -a n_x-\beta u & -a n_y-\beta v & -a n_z-\beta w & \beta & \phi\\ -e_V\tilde{\gamma}_r & \beta u e_V & \beta v e_V & \beta w e_V & -\beta e_V & a^2-\phi e_V\end{bmatrix}$$

$$L=\begin{bmatrix}\delta_{sr}/a^2 & 0 & 0 & c_s/2a^2 & c_s/2a^2 & 0\\ u/a^2 & l_x & m_x & (u+a n_x)/2a^2 & (u-a n_x)/2a^2 & 0\\ v/a^2 & l_y & m_y & (v+a n_y)/2a^2 & (v-a n_y)/2a^2 & 0\\ w/a^2 & l_z & m_z & (w+a n_z)/2a^2 & (w-a n_z)/2a^2 & 0\\ \left[\beta(u^2+v^2+w^2)-\tilde{\gamma}_r\right]/\beta a^2 & \tilde{V} & \tilde{W} & (H+a\tilde{U})/2a^2 & (H-a\tilde{U})/2a^2 & -\phi/\beta a^2\\ 0 & 0 & 0 & e_V/2a^2 & e_V/2a^2 & 1/a^2\end{bmatrix}$$

The eigenvalues of Jacobian matrix (42) are

$$\lambda_{1,2,5}=|\mathrm{k}|\tilde{U} \tag{43}$$

$$\lambda_3=|\mathrm{k}|(\tilde{U}+a) \tag{44}$$

$$\lambda_4=|\mathrm{k}|(\tilde{U}-a) \tag{45}$$

where subscript "s" refers to row s and species s, whereas subscript "r" refers to column r and species r. Both s and r vary from 1 to 5 in the present model. The unit vector n is defined from vector k as

$$\mathrm{n}=(n_x,n_y,n_z)=\frac{(k_1,k_2,k_3)}{|\mathrm{k}|} \tag{46}$$

$\mathrm{l}=\left(l_x,l_y,l_z\right)$ and $\mathrm{m}=\left(m_x,m_y,m_z\right)$ are two unit vectors such that n, l, and m are mutually orthogonal. Furthermore, we have,

$$\tilde{U}=un_x+vn_y+wn_z \tag{47}$$

$$\tilde{V}=ul_x+vl_y+wl_z \tag{48}$$

$$\tilde{W}=um_x+vm_y+wm_z \tag{49}$$

The derivative of pressure respecting to conservative variables comes from

$$dp = \beta(d\rho E - ud\rho u - vd\rho v - wd\rho w) + \phi d\rho e_V + \tilde{\gamma}_s d\rho_s \tag{50}$$

where

$$\beta = \frac{\bar{R}}{\rho \sum_s c_s c_{v,tr}^s} \sum_{r=1}^{5} \frac{\rho_r}{M_r} \tag{51}$$

$$\phi = \frac{\bar{R}}{\rho C_{v,V}} \frac{\rho_e}{M_e} - \beta \tag{52}$$

$$\tilde{\gamma}_s = \frac{\bar{R} T_q}{M_s} + \beta \frac{u^2 + v^2 + w^2}{2} - \beta e_s - \phi e_{V,s} \tag{53}$$

$$a^2 = \sum_{s=1}^{5} c_s \tilde{\gamma}_s + \beta \left[H - (u^2 + v^2 + w^2) \right] + \phi e_V = (1 + \beta) \frac{p}{\rho} \tag{54}$$

In equation (53), $T_q = T_V$ when s is an electron, otherwise, $T_q = T$.

In shock-fitting method, the velocity and location of the shock are solved as part of the solutions. The flow variables behind the shock are determined by Rankine-Hugoniot relations across the main shock and a characteristic compatibility relation from behind the shock. With the assumptions of "frozen" flow (no chemical reactions and energy relaxations when flow passes through the shock), the species mass fractions and vibration temperature keep constant on the two sides of the shock where translation temperature jumps across the shock. In this way, shock jumps conditions for total density, momentum and total energy are the same as those for perfect gas. In addition, the compatibility relation relating to the maximum eigenvalue in wall normal direction is used.

In the interior, compressible Navier-Stokes equations are solved in fully conservative form. An explicit finite difference scheme is used for spatial discretization of the governing equation, the inviscid flux terms are discretized by a fifth-order upwind scheme, and the viscous flux terms are discretized by a sixth-order central scheme. For the inviscid flux vectors, the flux Jacobians contain both positive and negative eigenvalues. A simple local Lax-Friedrichs scheme is used to split vectors into negative and positive wave fields. For example, the flux term F in Eq. (41) can be split into two terms of pure positive and negative eigenvalues as follows

$$F = F_+ + F_- \tag{55}$$

where $F_+ = \frac{1}{2}(F + \lambda U)$ and $F_- = \frac{1}{2}(F - \lambda U)$ and λ is chosen to be larger than the local maximum eigenvalue of F′.

$$\lambda = \frac{|\nabla \eta|}{J} \left(\sqrt{(\varepsilon c)^2 + u'^2} + c \right) \tag{56}$$

where

$$u' = \frac{\eta_x u + \eta_y v + \eta_z w + \eta_t}{|\nabla \eta|} \tag{57}$$

The parameter ε is a small positive constant added to adjust the smoothness of the splitting. The fluxes F_+ and F_- contain only positive and negative eigenvalues respectively. Therefore, in the spatial discretization, the derivative of the flux F is split into two terms

$$\frac{\partial F}{\partial \eta} = \frac{\partial F_+}{\partial \eta} + \frac{\partial F_-}{\partial \eta} \tag{58}$$

where the first term on the right hand side is discretized by the upwind scheme and the second term by the downwind scheme.

The fifth-order explicit scheme utilizes a 7-point stencil and has an adjustable parameter α as follows

$$u_i' = \frac{1}{hb_i}\sum_{k=-3}^{3} a_{i+k}u_{i+k} - \frac{\alpha}{6!b_i}h^5\left(\frac{\partial^6 u}{\partial x^6}\right)_i + \ldots \tag{59}$$

where $\alpha_{i\pm3} = \pm 1 + \frac{1}{12}\alpha,\ \alpha_{i\pm2} = \mp 9 - \frac{1}{2}\alpha,\ \alpha_{i\pm1} = \pm 45 + \frac{5}{4}\alpha,\ \alpha_i = -\frac{5}{3}\alpha$ and $b_i = 60$. The scheme is upwind when α < 0 and downwind when α > 0. It becomes a 6-order central scheme when α = 0 which is used for discretizing viscous terms. All our methods are coded based on message passing interface (MPI) is used for communication in the parallel computations.

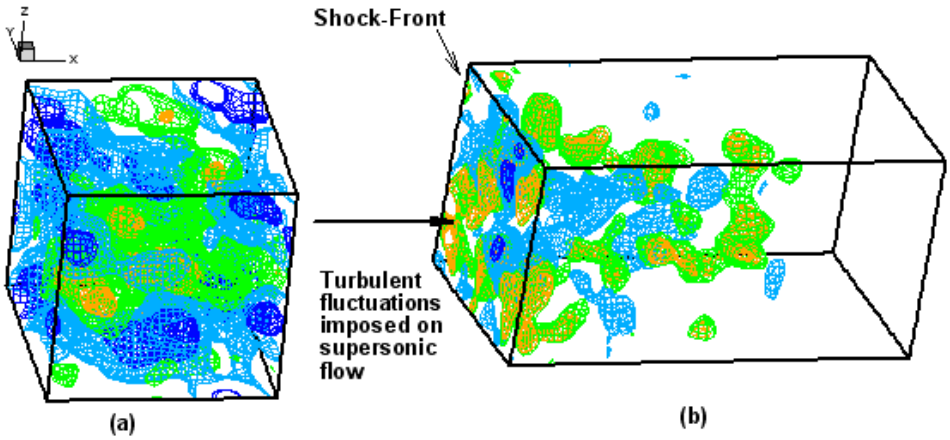

Fig. 5. Schematic showing typical density contours and computational domains for simulation of shock-turbulence interaction using shock-fitting algorithm [1].

For the problem shown in Fig. 1, there is no need for the shock-fitting algorithm to solve the supersonic flow upstream of the shock. Hence, computational domain for the shock-fitting method for shock and turbulence interaction consists of flow only downstream of the shock. The supersonic turbulent flow ahead of the shock can be computed in a separate simulation. A schematic of the shock-fitting implementation for the shock-turbulence interaction problem is shown in Fig. 5. The inflow turbulence is generated using a separate direct numerical simulation as shown in Fig. 5(a). We compute decaying isotropic turbulence in a periodic box to generate the realistic turbulent fluctuations that can be used as incoming turbulence for the shock-fitting algorithm. The computational domain for implementation of shock-fitting algorithm is shown in Fig. 5(b). The shock front forms the left boundary of the computational domain.

The turbulent fluctuations generated from Fig. 5(a) are imposed on supersonic flow and used as inflow condition at the shock following the Taylor's hypothesis that is valid for small turbulent intensities ($M_t < 0.5$ and $u'_{1rms}/\bar{u}_1 < 0.15$) [38]. For higher turbulent intensities, it is advisable to carry out simulation of spatially decaying turbulence which is more expensive. From the temporal simulations inside a periodic box, we obtain values of flow variables at fixed grid points

of the box. Moreover, when the turbulent box is convected through the shock in the shock-fitting computations, the shock-points generally do not align with grid points of the turbulent box. Hence, values on the supersonic side of the shock are computed using interpolations. Since in our shock-fitting formulation the grids move in only one direction (X-direction in Fig. 5(b)), one dimensional Fourier interpolation is sufficient for this purpose. As a boundary condition, shock-fitting formulation needs the values of the time derivatives of conservative variables ahead of the shock according to the isotropic field which using Taylor's hypothesis are taken as appropriate spatial derivatives. Together with one characteristic coming to the shock from the high pressure side, these values determine the time derivatives at the downstream side. Thus, they are calculated from the corresponding upstream values, using the Rankine–Hugoniot conditions. Periodic boundary conditions are used in the transverse directions and non-reflecting characteristic boundary conditions are used at the subsonic exit of the computational domain.

3. Strong shock and turbulence interaction

The extensive DNS studies on strong shock and turbulence interaction of perfect gas flow are similar to those of Rawat and Zhong [29]. The main objective is to obtain more quantitative results. Therefore, validation of the shock-fitting method and grid convergence of DNS results are neglected in the current paper.

3.1 Decaying isotropic turbulence in the periodic box

Simulation of decaying isotropic turbulence in a periodic box is started with initial conditions generated using the algorithm given by Erlebacher et al [39]. The algorithm is based on generating random fields for fluctuations of flow variables and imposing a given spectrum. Following spectrum is imposed on the fluctuations of flow variables,

$$E(k) \propto k^4 \exp\left[-2\left(k/k_0\right)^2\right] \tag{60}$$

where $k = \sqrt{k_1^2 + k_2^2 + k_3^2}$ is the wave number of fluctuation and k_0 is the most energetic wave number. Figure 6 shows the energy spectra of fluctuations of flow variables before and after imposing the prescribed spectra. The fluctuation shown in Fig. 6(b) is used as initial conditions for the inflow simulation. This method offers flexibility to generate various turbulent regimes.

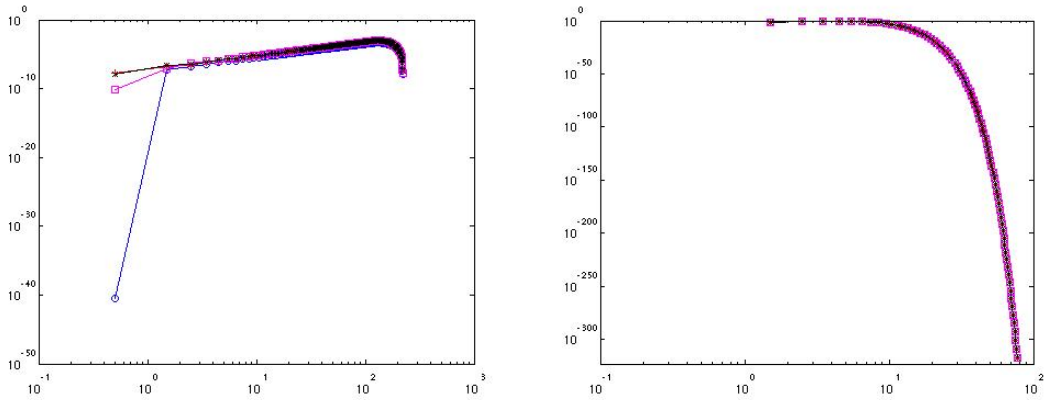

(a) random fluctuations *(b) scaled fluctuations*

Fig. 6. Spectra of fluctuations of flow variables.

The most important parameters that govern the physics of shock and turbulence interactions are turbulent Mach number M_t and Reynolds number based on Taylor microscale λ. These quantities are defined as follows:

$$M_t = q/\bar{c} \tag{61}$$

$$\mathrm{Re}_\lambda = \bar{\rho} u_{rms} \lambda / \bar{\mu} \tag{62}$$

where,

$$q = \left(\widetilde{u_i'' u_i''} \right)^{\frac{1}{2}} \tag{63}$$

For any given variable f, $\bar{f}$ denotes an ensemble average and $\tilde{f}$ is mass-weighted average i.e. $\tilde{f} = \overline{\rho f}/\bar{\rho}$. Deviations from ensemble average and mass-weighted average are denoted as f' and f'', respectively. Subscript '1' has been used to denote the quantities upstream of the shock. Speed of sound is denoted as c, $u_{rms} = \left(\widetilde{u_1''^2} \right)^{1/2}$ and Taylor microscale is $\lambda = \left(\lambda_1 + \lambda_2 + \lambda_3 \right)/3$ where

$$\lambda_\alpha = \left[\overline{u'^2_\alpha} \Big/ \overline{\left(\frac{\partial u'_\alpha}{\partial x_\alpha} \right)^2} \right]^{1/2} \qquad (\alpha = 1, 2 \text{ or } 3) \tag{64}$$

The following dimensionless parameters are used as initial condition for generating initial random fluctuations: upstream mean density, $\rho_1 = 1$, temperature $T_1 = 1$, initial rms value of velocity fluctuations $u^0_{rms} = 1$, $\mathrm{Pr} = 0.7$, $\gamma = 1.4$. The values of initial turbulent Mach number, M_{t0}, and initial Reynolds number, $\mathrm{Re}_{\lambda 0}$ are given. Non-dimensionalized gas constant is given by $R = 3/\gamma M^2_{t0}$ and reference viscosity is given as $\mu_0 = \rho_1 u^0_{rms} \lambda_0 / \mathrm{Re}_{\lambda,0}$ $\lambda_0 = 2/k_0$.

The initial conditions are assigned in a box of dimension $(2\pi)^3$ and compressible Navier-stokes equations are solved using periodic boundary conditions in all three directions until reasonably realistic turbulence is achieved. Skewness of velocity derivatives is a measure of inertial non-linearity of turbulence. Skewness of streamwise velocity derivatives is an important parameter to be monitored during the simulation of decaying isotropic turbulence, which is defined as follows,

$$S_1 = \overline{\left(\partial u_1' / \partial x_1 \right)^3} \Big/ \overline{\left[\left(\partial u_1' / \partial x_1 \right)^2 \right]}^{3/2} \tag{65}$$

For the parameters considered here, a realistic turbulence should have S_1 in the range -0.4 to -0.6 [9, 24, 25]. In all of our calculations of inflow turbulence we found that S_1 reaches steady state in $t \sim \lambda_0 / u^0_{rms}$. Figures 7 and 8 show variations of various statistics obtained from simulations for flow with initial parameters $M_{t0} = 0.175$ and $\mathrm{Re}_{\lambda 0} = 135$, and $M_{t0} = 0.15$ and $\mathrm{Re}_{\lambda 0} = 50$, respectively. These computations were performed with 256^3 grid points. Apart from S_1, we also plot turbulent Mach number, M_t, variance of velocity fluctuations, Reynolds number based on

Taylor microscale, Re_λ, and variance of dilatation fluctuations, $d = \partial u_i / \partial x_i$. It can be seen that velocity fluctuations are dissipated with the time, leading to decay in turbulent Mach number as well as Taylor microscale. Sudden increase in dilatation is due to completely solenoidal initial conditions and has been reported in previous studies as well [40, 41].

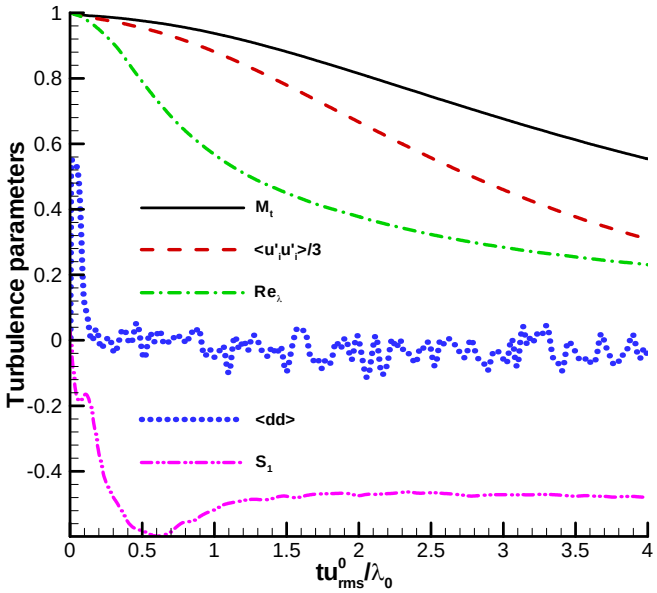

Fig. 7. Variation of various turbulence statistics in simulation of decaying isotropic turbulence $(M_{t0} = 0.175, \mathrm{Re}_{\lambda 0} = 135)$.

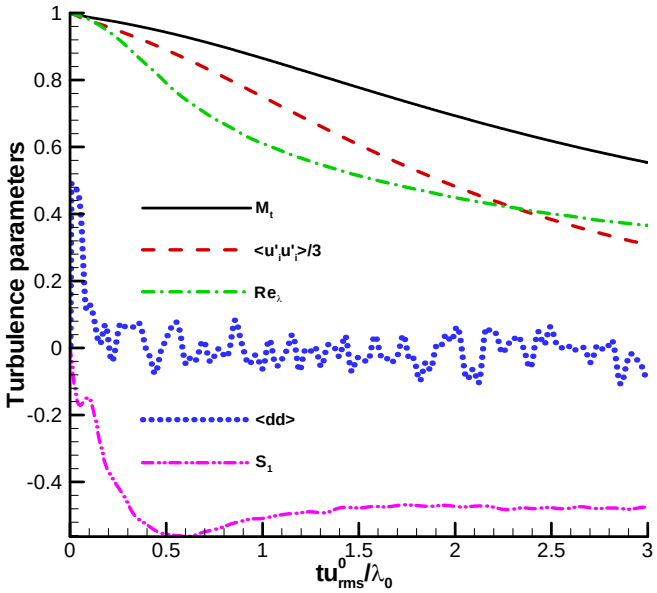

Fig. 8. Variation of various turbulence statistics in simulation of decaying isotropic turbulence $(M_{t0} = 0.15, \mathrm{Re}_{\lambda 0} = 50)$.

After the skewness of velocity derivative, S_1, becomes steady to have a value between -0.4 and -0.6, we choose a flow-field with desired values of M_t and Re_λ as inflow condition for the shock-fitting computations. One can vary the flow conditions of decaying isotropic turbulence to obtain well developed realistic turbulence with desired statistical properties.

3.2 Statistics of shock and turbulence interaction

We compute 4 series of DNS computations with varying incoming flow of turbulence intensities M_t from 0.083 to 0.143, mean Mach number from 2 to 30, and Reynolds number, Re_λ, from 18.9 to 52.4. Inflow conditions of Cases I & II are obtained from the decaying isotropic turbulence computation with initial parameters $M_{t0} = 0.175$ and $\mathrm{Re}_{\lambda 0} = 135$ at tu^0_{rms}/λ_0 = 2.0 and 3.0 as shown in Fig. 7. Whereas inflow conditions of Cases III & IV are obtained from the decaying isotropic turbulence computation with initial parameters $M_{t0} = 0.15$ and $\mathrm{Re}_{\lambda 0} = 50$ at tu^0_{rms}/λ_0 = 2.0 and 3.0 as shown in Fig. 8.

Table 3. Four cases of inflow conditions used in DNS of shock and turbulence interaction

	M_1	M_t	Re_λ	Grids
Case I	2 - 30	0.143	52.4	256×256×512
Case II	2 - 30	0.118	39.4	256×256×512
Case III	2 - 30	0.104	23.1	256×256×512
Case IV	2 - 30	0.083	18.9	256×256×512

The computational domain for DNS of shock and turbulence interaction is schematically shown in Fig. 5(b). The shock forms the left boundary of the computational domain. The turbulent fluctuations generated from Fig. 5(a) on a periodic box of dimensions $2\pi^3$ are imposed on supersonic flow and used as inflow condition at the shock. For shock-fitting computations, we use a domain of size $4\pi \times 2\pi^2$ and same non-dimensionalization of flow variables is used. Uniform conditions corresponding to laminar Rankine-Hugoniot jump conditions are used as initial condition for simulation of post-shock flow. As the shock interacts with the incoming turbulence, transient features are generated. Several flow-through of inflow box are needed before turbulence statistics in post-shock flow reach a steady state.

It is observed from previous shock-turbulence interaction simulations that turbulent fluctuations are generally much stronger just behind the shock. Hence, it is advisable to cluster more grid points near the shock. The grid-spacing in transverse direction is determined by the lengthscales in DNS of turbulent flow. For simulation of isotropic flows, it has been suggested that one should resolve a wavelength of $4.5\eta_s$ where η_s is the Kolmogorov length scale for the flow in the computational domain [42]. With our fifth-order finite-difference scheme such resolution will require a grid spacing of $2.0\eta_s$ in transverse direction. On the upstream side of the shock, the Kolmogorov length scale is defined as $\eta_0 \approx 0.51\lambda/\sqrt{\mathrm{Re}_\lambda}$. Larsson and Lele [43] have recently presented a relation for the change in the Kolmogorov length scale across the shock which leads to $\eta_s \approx \eta_0 (\rho_s/\rho_u)^{-11/8} (p_s/p_u)^{3/8}$ [28]. With $\lambda \approx 2/k_0$, about $6.1 k_0 \sqrt{\mathrm{Re}_\lambda} (\rho_s/\rho_u)^{11/8} (p_s/p_u)^{-3/8}$ grids are needed in transverse directions. Based on these requirements, we chose to use 256 grid points in transverse direction.

For the computations of statistics, we need averaging over transverse directions as well as in time as the turbulence behind the shock is stationary and homogeneous. We found that storing and computing averages from 60 instantaneous flow-fields during time interval T is necessary for statistical convergence, where T represents the time needed for the inflow passing through one length of periodic box. Figure 9 shows the streamwise-streamwise Reynolds Stress, $R_{11} = \widetilde{u_1'' u_1''}$, computed for one flow-through of inflow box at several different time. These calculations are for inflow conditions of $M_1 = 30$, $M_t = 0.143$ and $\mathrm{Re}_\lambda = 52.4$. All of these cases used 60 snapshots for averaging the statistics.

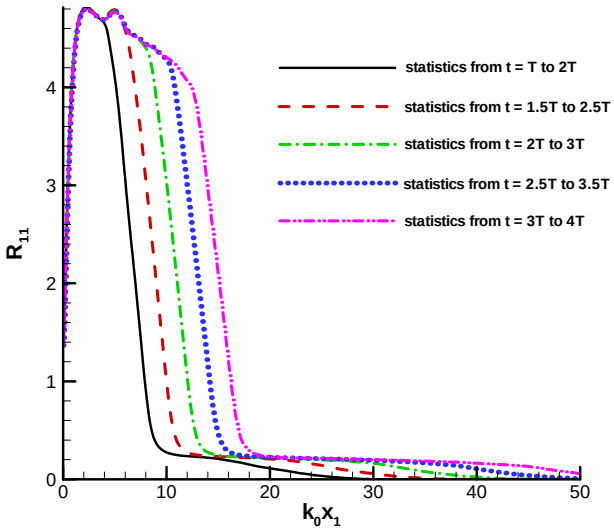

Fig. 9. The streamwise-streamwise Reynolds stress computed using 60 snapshots of flow-fields at different points in time (case I, $M_1 = 30$).

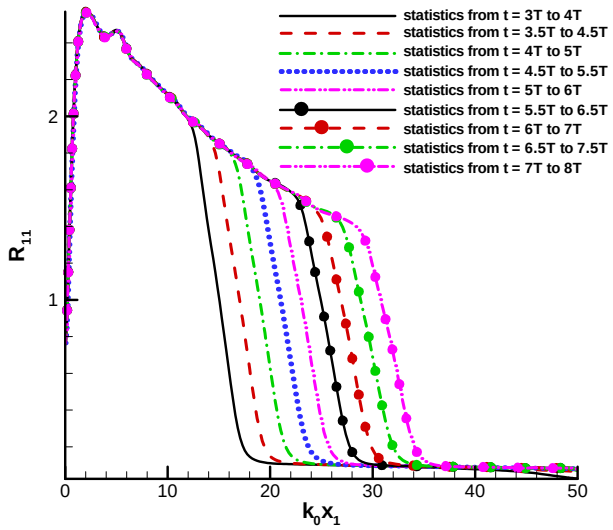

Fig. 10. The streamwise-streamwise Reynolds stress computed using 60 snapshots of flow-fields at different points in time (case III, $M_1 = 30$).

It can be seen that statistics reach steady state in longer region behind the shock wave as time progresses. The steady state is achieved in a region of length $14/k_0$ behind the shock after 4 flow-through of the inflow. Similar statistics of the streamwise-streamwise Reynolds Stress for inflow conditions of $M_1 = 30$, $M_t = 0.104$ and $\mathrm{Re}_\lambda = 23.1$ are shown in Fig. 10. Again, it is observed that statistics reach steady state in longer region behind the shock wave as time progresses. We obtain steady state in a region of length $30/k_0$ behind the shock after 8 flow-through of the inflow.

3.3 Fluctuation of shock front

In shock and turbulence interaction, the shock gets distorted. We plot RMS values of the fluctuations in streamwise coordinate, x_{rms}, in Fig. 11 for case I computations. Here, $k_0x_1 = 0$ represents the shock whereas $k_0x_1 \approx 50$ represents the exit boundary of the computational domain. It is the fluctuation of shock front at $k_0x_1 = 0$ that leads to the fluctuations of streamwise coordinate. After that, fluctuations of streamwise coordinate keep decreasing until they go to zero at the exit boundary. Figure 11 shows that the increase in shock strength reduces shock deformation. The result is quite reasonable. For fixed freestream isotropic turbulence, it is much difficult to distort a stronger shock. Similar results are obtained from other three cases.

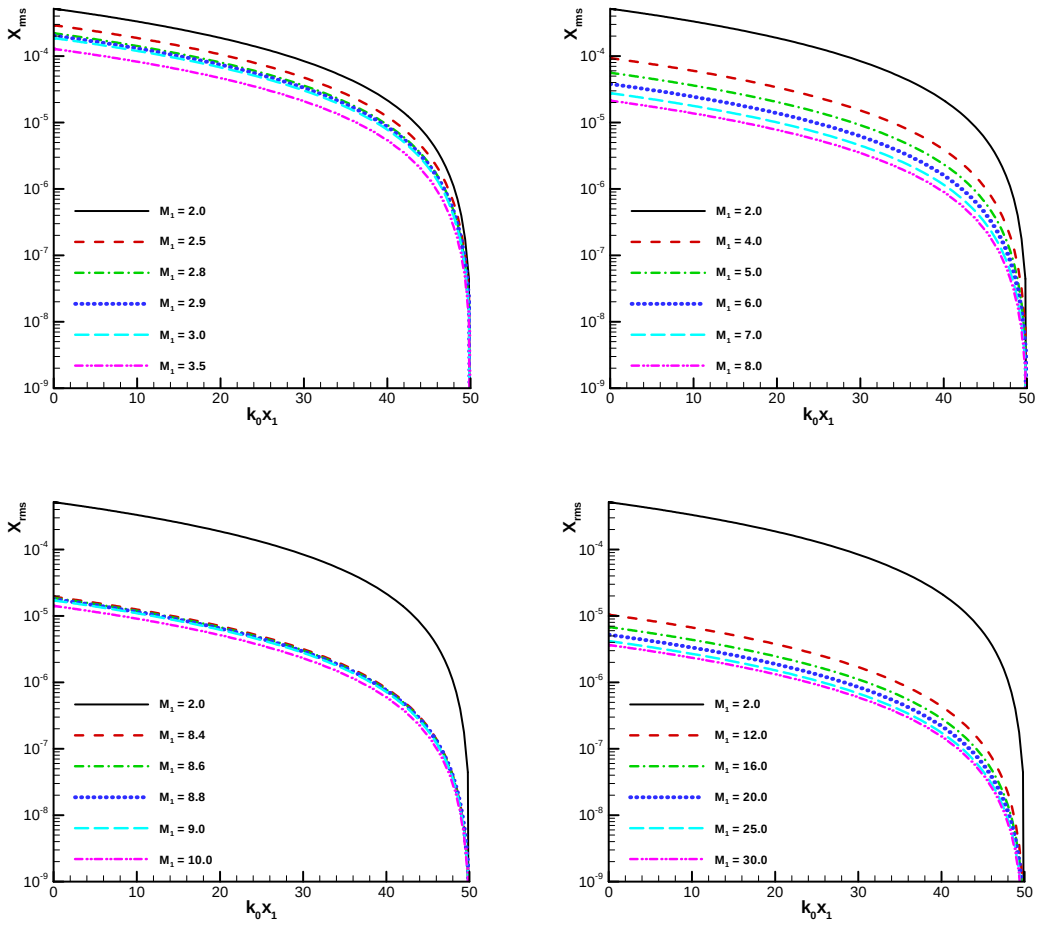

Fig. 11. Root mean square values of fluctuations in streamwise coordinate (case I).

Figure 12 compares RMS values of the fluctuations in streamwise coordinate at a given shock Mach number for the four cases of computations. Again, the figure shows that the increase in shock strength reduces shock deformation, as the fluctuation of shock front in Fig. 12(b) is two orders of magnitude smaller than that in Fig. 12(a). For a given shock Mach number, the fluctuation of shock front is reduced from case I to case IV, because the strength of freestream isotropic turbulence decreases.

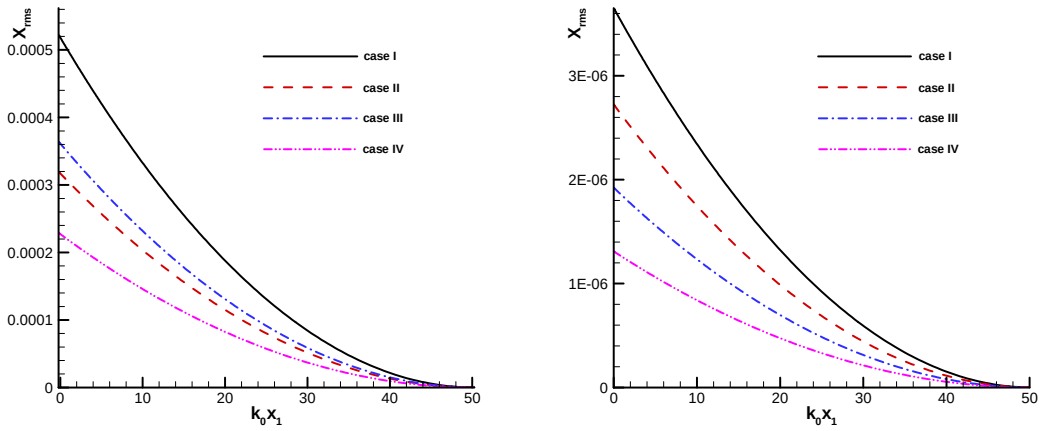

(a) $M_1 = 2.0$ *(b) $M_1 = 30.0$*

Fig. 12. Root mean square values of fluctuations in streamwise coordinate at a given shock Mach number.

The above results seem to be quite straightforward, because it is easy for the shock-fitting method to get the location and fluctuation of the shock front. But it will be very difficult for shock-capturing schemes to evaluate the fluctuation of shock front.

3.4 Mean flow

For the post-shock flows, the linear theory results assume fluctuations around the mean values given by Rankine-Hugoniot jump conditions. Lele [44] used results of rapid distortion theory to find shock-jump relations in turbulent flows. A drift velocity in normal shock moving through a turbulent flow was found to be necessary to sustain the laminar density ratio corresponding to the stationary shock. This corresponds to a smaller jump in mean density and pressure of turbulence flow across the shock than that predicted by jump conditions.

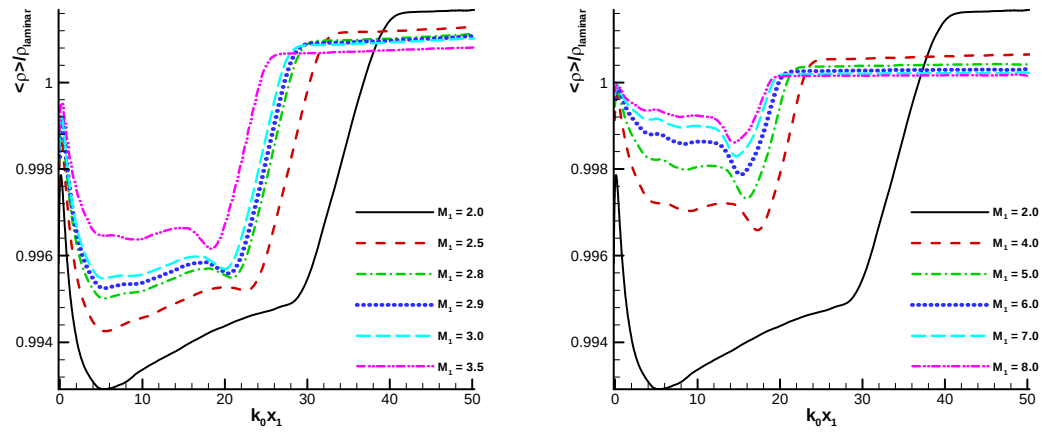

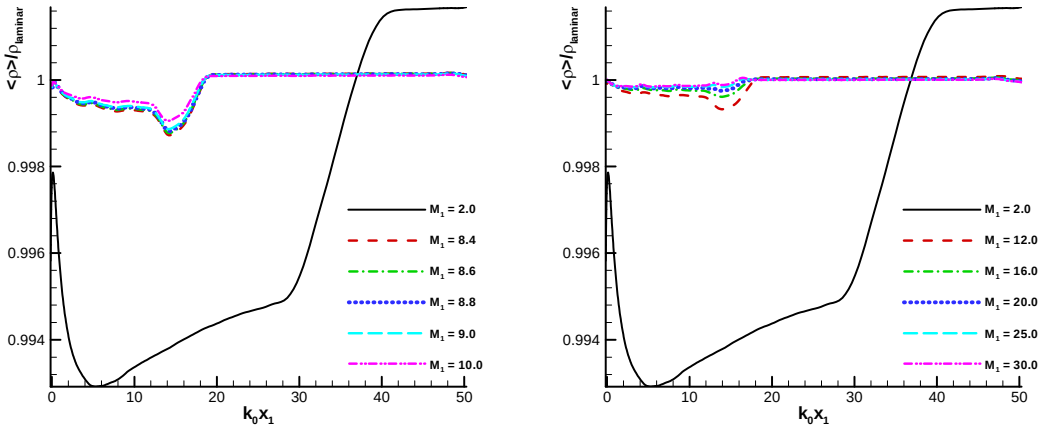

Fig. 13. Mean values of density behind the shock for inflow conditions of case I.

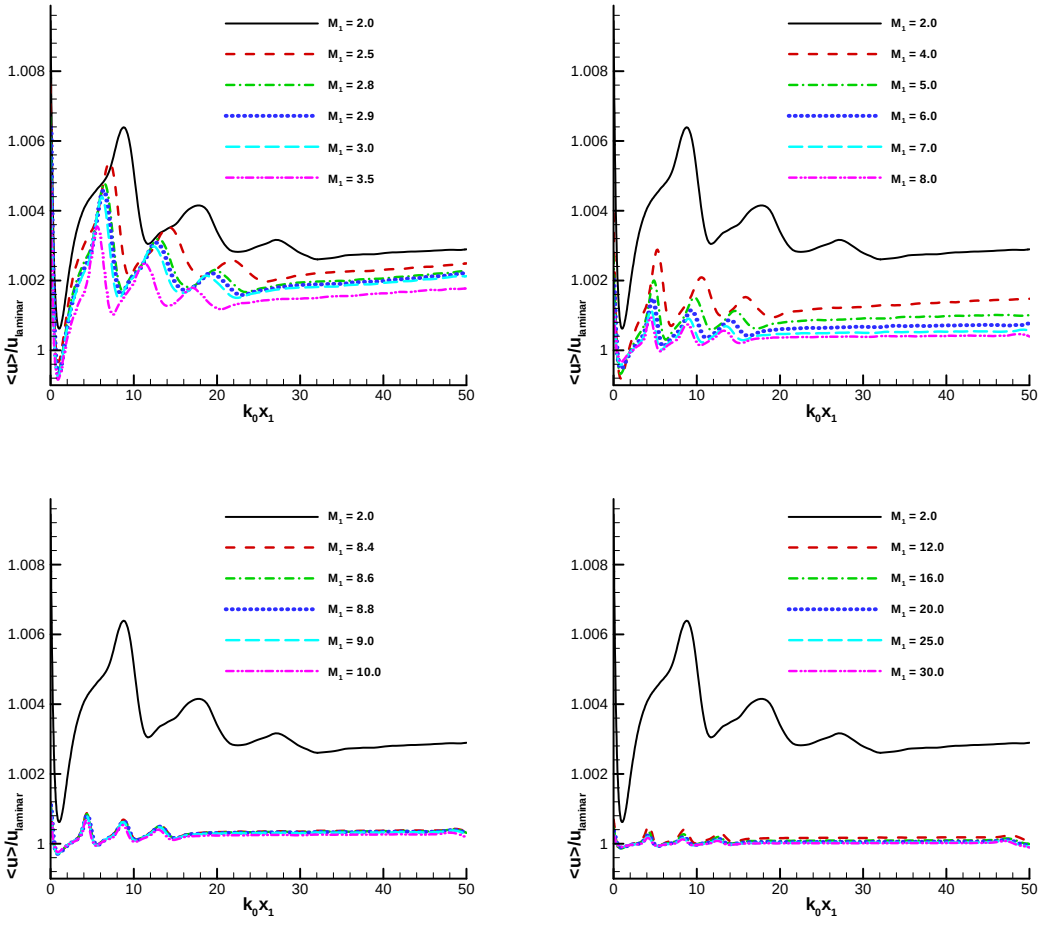

Fig. 14. Mean values of streamwise velocity behind the shock for inflow conditions of case I.

In Figs. 13 and 14, we present the profiles of density and streamwise velocity behind the shock for inflow conditions of case I. Just downstream of the shock, mean values change rapidly. It is observed that mean density behind the shock is lower than that in corresponding laminar flow,

which is consistent with those reported in the literature [43]. Mean streamwise velocity first decreases and then increases. We also observe in Figs. 13 and 14 that as mean Mach number value of incoming flow increases at fixed values of turbulent Mach number and Reynolds number, the difference between laminar and turbulent post-shock mean values decreases.

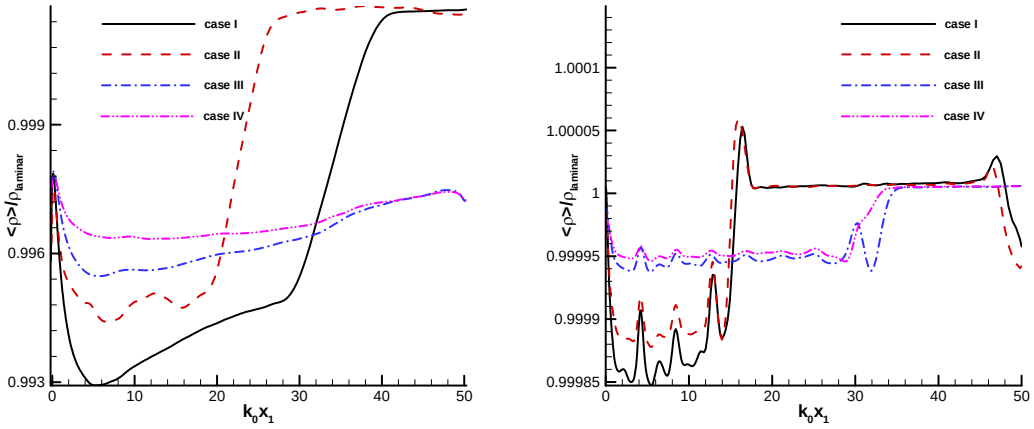

(a) M_1 = 2.0 *(b) M_1 = 30.0*

Fig. 15. Mean values of density behind the shock at a given shock Mach number.

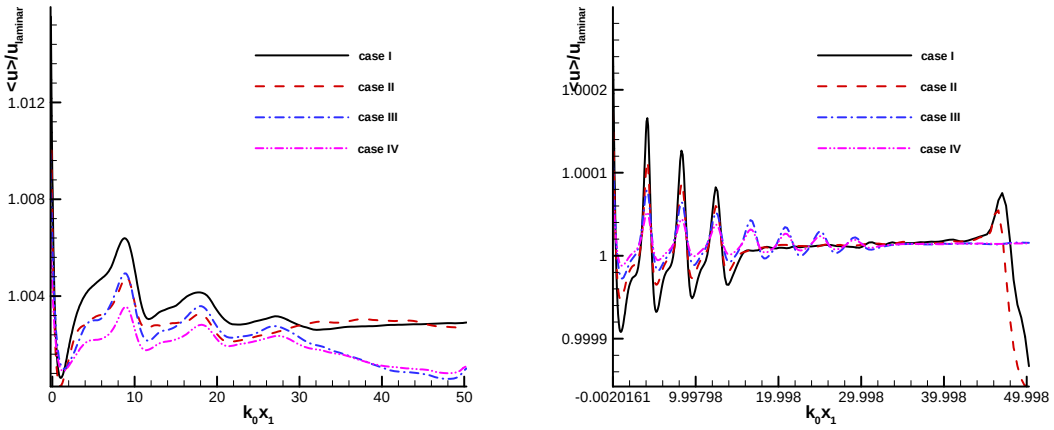

(a) M_1 = 2.0 *(b) M_1 = 30.0*

Fig. 16. Mean values of streamwise velocity behind the shock at a given shock Mach number.

Figure 15 compares mean values of density behind the shock at a given shock Mach number for the four cases of computations. The figure shows that the increase in shock strength reduces the difference between mean density and its laminar counterpart, as the decrease of mean density right after the shock in Fig. 15(b) is also two orders of magnitude smaller than that in Fig. 15(a). For a given shock Mach number, the decrease of mean density right after the shock is reduced from case I to case IV as the strength of freestream isotropic turbulence decreases. Similar results are shown in Fig. 16, where the mean values of streamwise velocity behind the shock at a given shock Mach number are compared for the four cases of simulations.

3.5 Vorticity variance

For the quasi-incompressible inflow turbulence, one of the most important contributions to the dissipation of turbulent kinetic energy is expected from the vorticity fluctuations. Linear interaction analysis predicts an increase in the transverse vorticity values which is expected to remain constant downstream of the shock. Amplitude of streamwise vorticity fluctuations is expected to remain unchanged throughout the computational domain. We observe these trends at the shock. However, downstream of the shock considerable non-linear effects are observed since both streamwise and transverse vorticity values change significantly moving away from the shock.

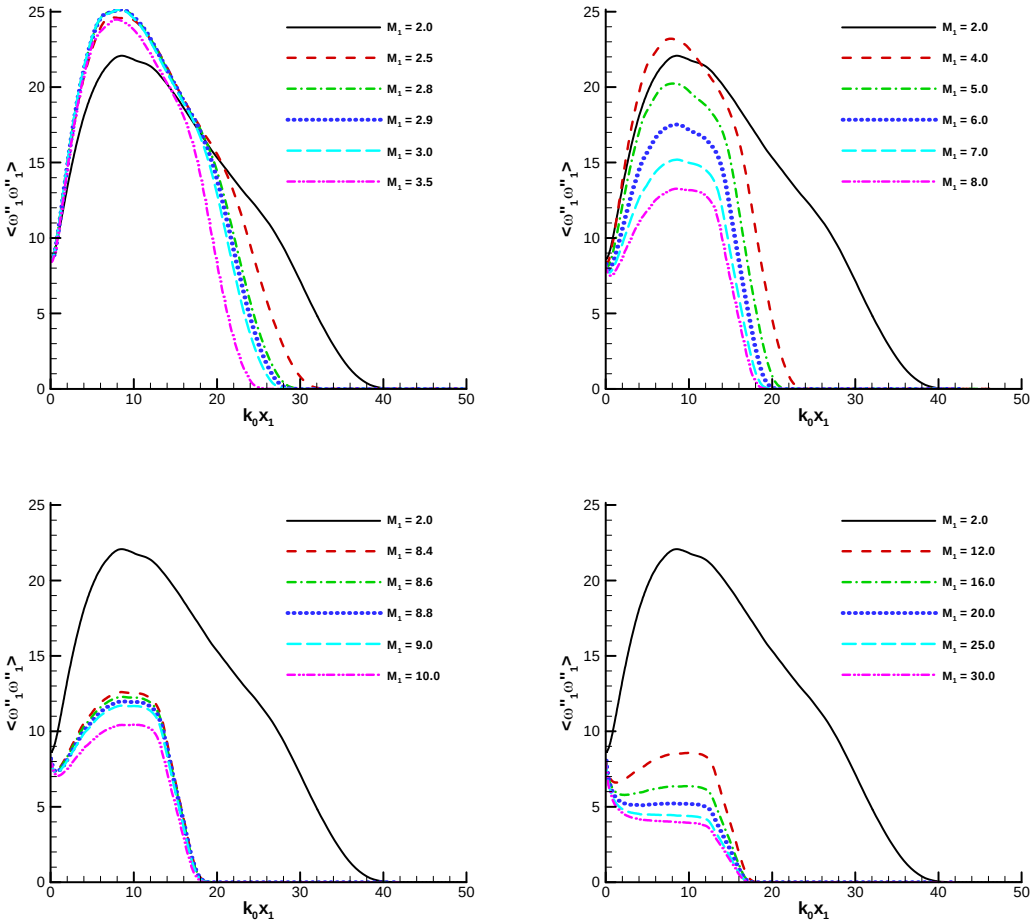

Fig. 17. Effect of increasing mean Mach number on the variance of streamwise vorticity for inflow conditions of case I.

Evolutions of variance in streamwise vorticity fluctuations, $\widetilde{\omega_1''\omega_1''}$, is presented in Figs. 17 and 18 with the varying shock strengths but using same inflow turbulence of case I and case III, respectively. Figure 17 shows that, for weaker than Mach 12 shocks in case I, streamwise vorticity increases behind the shock. In case III, Figure 18 shows that, for weaker than Mach 7 shocks, streamwise vorticity increases behind the shock. Such increase is attributed to the non-linear tilting and stretching of vorticity and has also been reported in the past studies [7, 43]. Both figures show that maximum values of variance of streamwise vorticity fluctuations first increase

and then decrease as the shock strength is increased. Furthermore, the peak of streamwise vorticity fluctuations is observed for shock and turbulence interactions with Mach 2.8 shock. In past, researchers [7, 43] considered weaker than Mach 3 shocks for such comparisons and concluded that effect of increasing shock strength is to simply increase the amplification of streamwise vorticity fluctuations. Although our results agree to these trend for lower Mach numbers, we see that for stronger than Mach 2.8 flows there is a decrease in streamwise vorticity. It is observed that non-linear tilting and stretching is suppressed by the viscous dissipation and streamwise vorticity continuously decreases downstream of the shock for stronger than Mach 12 shocks in Case I and for stronger than Mach 7 shocks in Case III. Therefore, the suppression of vorticity tilting and stretching in post-shock flow strongly depends on the inflow conditions.

The results of case II are quite similar to those of case I. And the results of case IV are quite similar to those of case IV. Because of the decrease of freestream isotropic turbulence from case I to case IV, the variances in streamwise vorticity fluctuation of case II and case IV are lower than those of case I and case III, respectively.

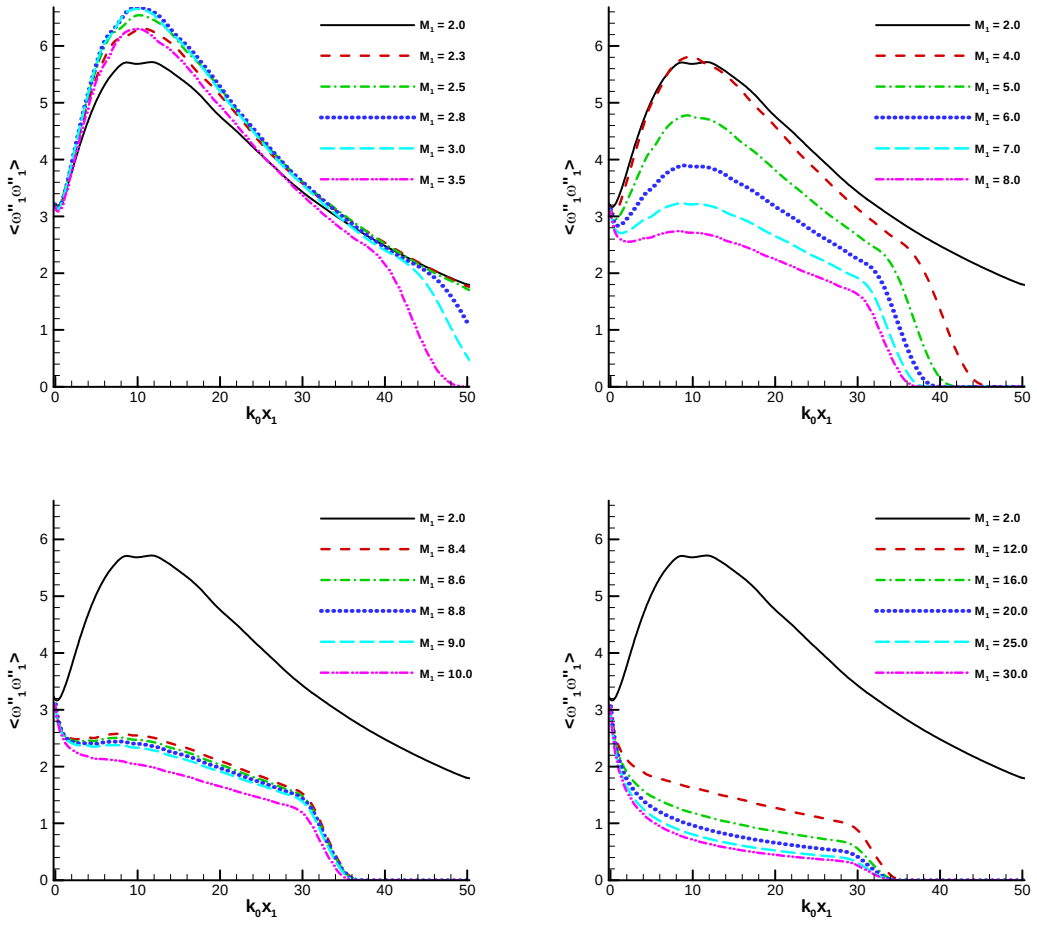

Fig. 18. Effect of increasing mean Mach number on the variance of streamwise vorticity for inflow conditions of case III.

Figure 19 compares the variances of streamwise vorticity at a given shock Mach number for the four cases of computations. These figures clearly demonstrated that DNS results of case II and

case IV are similar to those of case I and case III except that vorticity variances in case II and case IV have a low value. For each case, the maximum vorticity variance is achieved at $M_1 = 2.8$. In Figs. 19(a) and 19(b), vorticity variance of all the four cases initially increases then decreases after reaching a maximum. In Fig. 19(c), only the vorticity variances of cases I and II have an initial increase after the shock. In Fig. 19(d), vorticity variance of all the four cases decreases monotonically after the shock. Such results are consistent with Figs. 17 and 18. Specifically, streamwise vorticity increases behind the shock for weaker than Mach 12 shocks in case I. In case III, streamwise vorticity increases behind the shock for weaker than Mach 7 shocks.

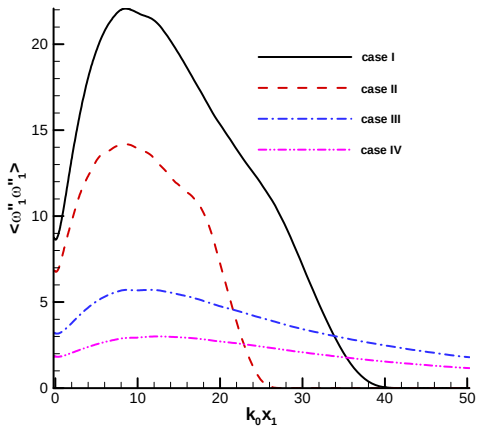

(a) $M_1 = 2.0$

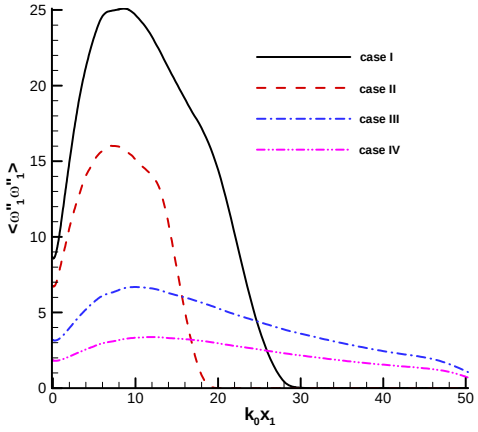

(b) $M_1 = 2.8$

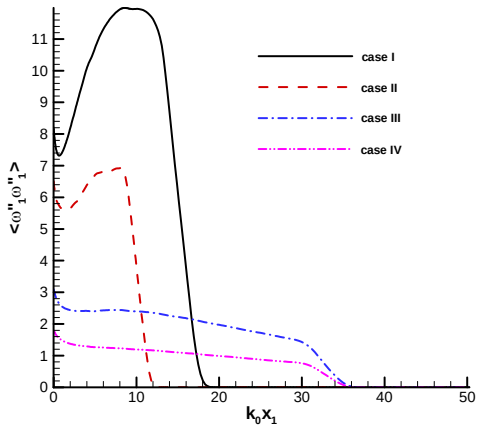

(c) $M_1 = 8.8$

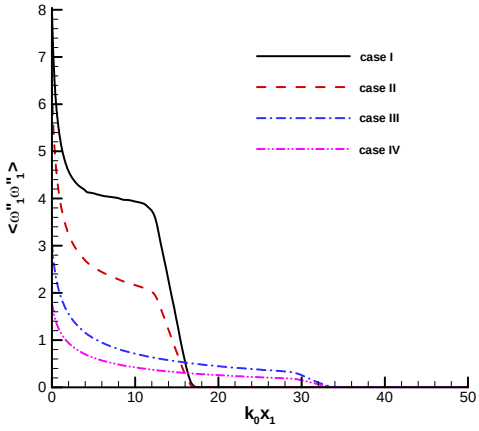

(d) $M_1 = 30.0$

Fig. 19. Variance of streamwise vorticity fluctuations at a given shock Mach number.

3.6 Reynolds stress R_{11}

Linear interaction analysis predicts that the amplification in turbulent kinetic energy saturates for stronger than Mach 3 shocks. Moreover, amplification of variance of streamwise-streamwise Reynolds stresses, R_{11}, is expected to decrease beyond Mach 3 shocks. We varied mean Mach number of the incoming flow from 2 to 30 for all cases of inflow conditions to see the effect of shock Mach number on shock and turbulence interactions.

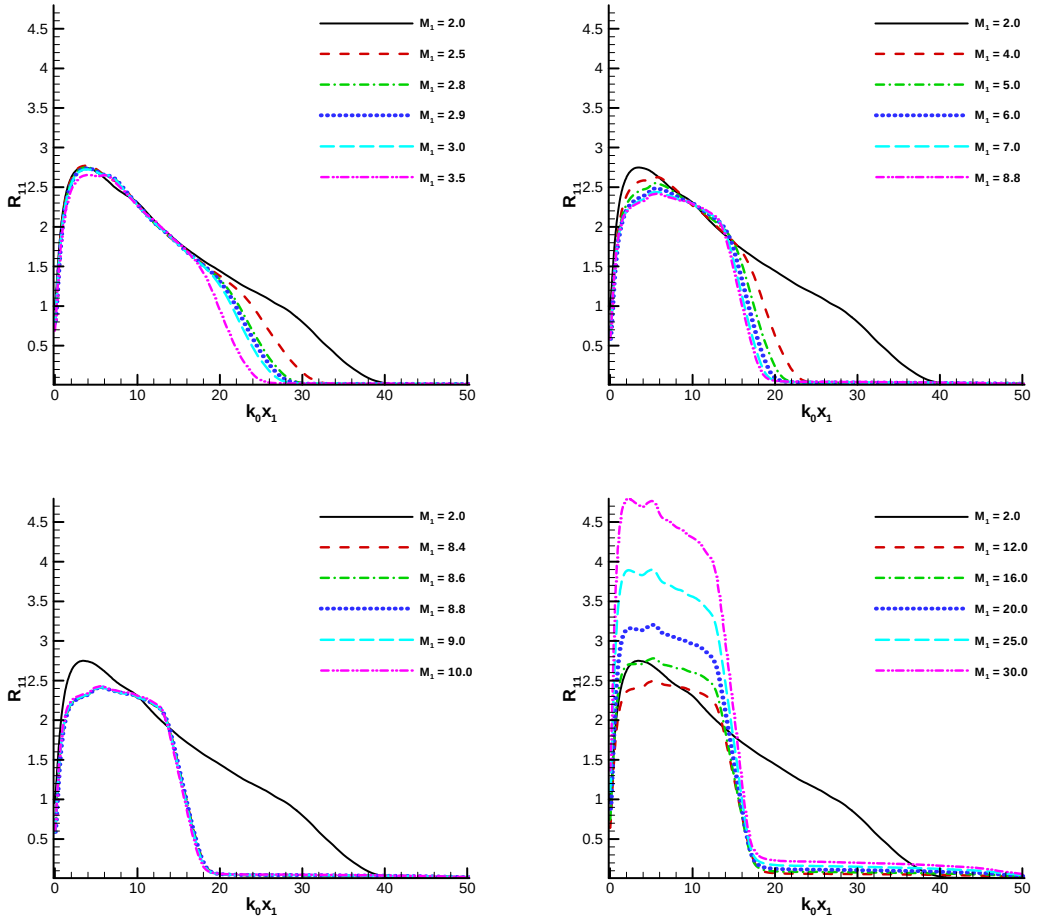

Fig. 20. Evolutions in streamwise-streamwise Reynolds stresses for inflow conditions of case I.

Streamwise variation of R_{11} for various shock strengths is shown in Fig. 20 for inflow conditions of case I. In general, the R_{11} values evolve rapidly behind the shock for all the shock strengths considered and reach maximum value before $x_1 = 10/k_0$. It is observed that maximum amplification of Reynolds stress R_{11} decreases as the Mach number of the mean flow is increased till 8.8. The decrease in R_{11} is consistent with findings of linear interaction analysis. This trend, however, reverses as shock strength is increased beyond Mach 8.8. For stronger than Mach 8.8 shocks, the Reynolds stress R_{11} is amplified as mean Mach number is increased. Similar conclusion can be drawn in Fig. 21, where streamwise variation of R_{11} for various shock strengths for inflow conditions of case III is shown. The only difference between Figs. 20 and 21 is the magnitude of Reynolds stress. Due to the weaker freestream isotropic turbulence, the magnitude of Reynolds stress in Fig. 21 is smaller than its counterpart in Fig. 20.

Again, the results of case II are quite similar to those of case I. And the results of case IV are quite similar to those of case IV. Because of the decrease of freestream isotropic turbulence from case I to case IV, streamwise-streamwise Reynolds stresses of case II and case IV are lower than those of case I and case III, respectively.

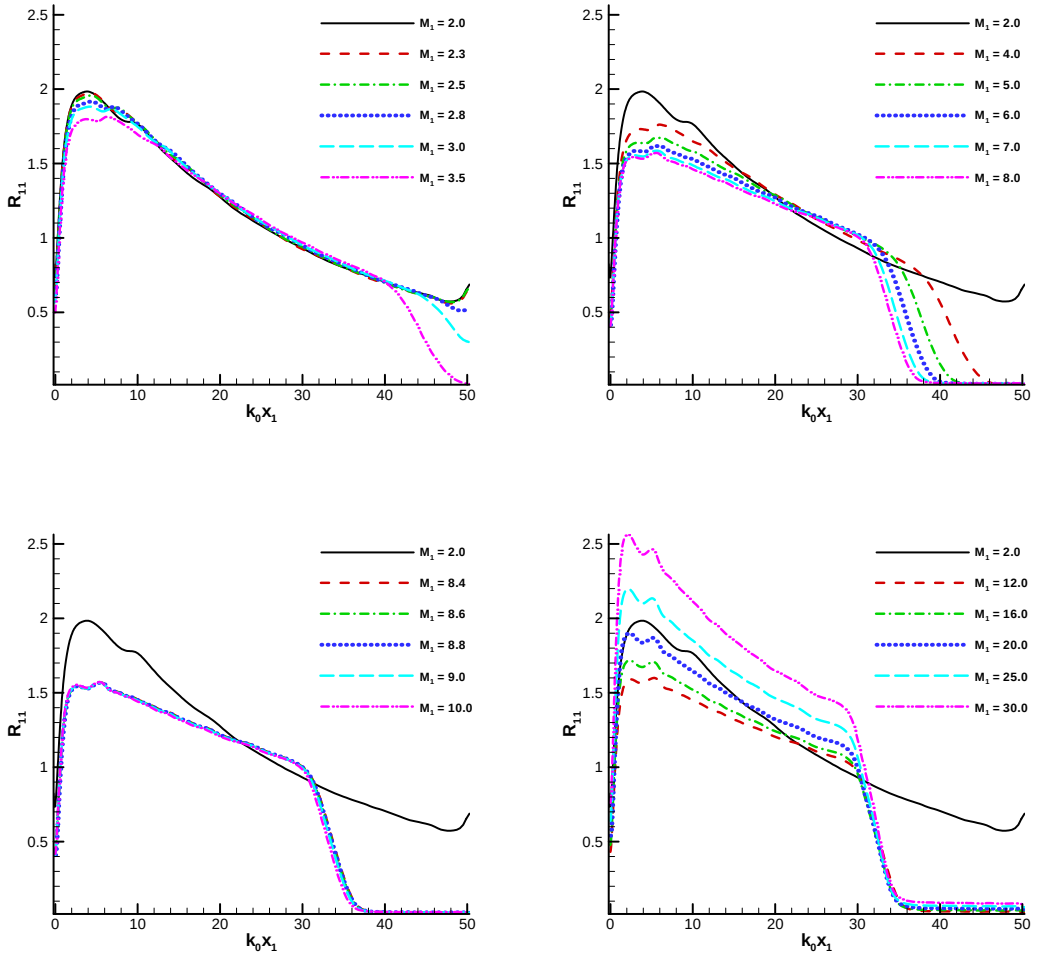

Fig. 21. Evolutions in streamwise-streamwise Reynolds stresses for inflow conditions of case III.

Figure 22 compares the evolutions in streamwise-streamwise Reynolds stresses at a given shock Mach number for the four cases of computations. These figures clearly demonstrated that DNS results of case II and case IV are similar to those of case I and case III except that Reynolds stresses in case II and case IV have a low value. For each case, the Reynolds stresses increase rapidly right after the shock. After reaching the maximum at around $x_1 = 4/k_0$, Reynolds stresses of cases I to III decrease. In case 4, the Reynolds stresses reach the maximum around $x_1 = 2/k_0$. It seems that the location of maximum Reynolds stresses move upstream for the really strong shock $M_1 = 30$. Figure 22 also shows that the peak of Reynolds stresses has the largest value in case I and the smallest value in case IV.

In Figs. 22(a) to 22(c), the Reynolds stresses of case II are smaller than those of case III. In Fig. 22(d), the Reynolds stresses of case II are larger than those of case III. Figs. 22(b) to 22(c) clearly show that maximum amplification of Reynolds stress R_{11} decreases as the Mach number of the mean flow is increased till 8.8. This trend, however, reverses as shock strength is increased beyond Mach 8.8. For stronger than Mach 8.8 shocks, the Reynolds stress R_{11} is amplified as mean Mach number is increased.

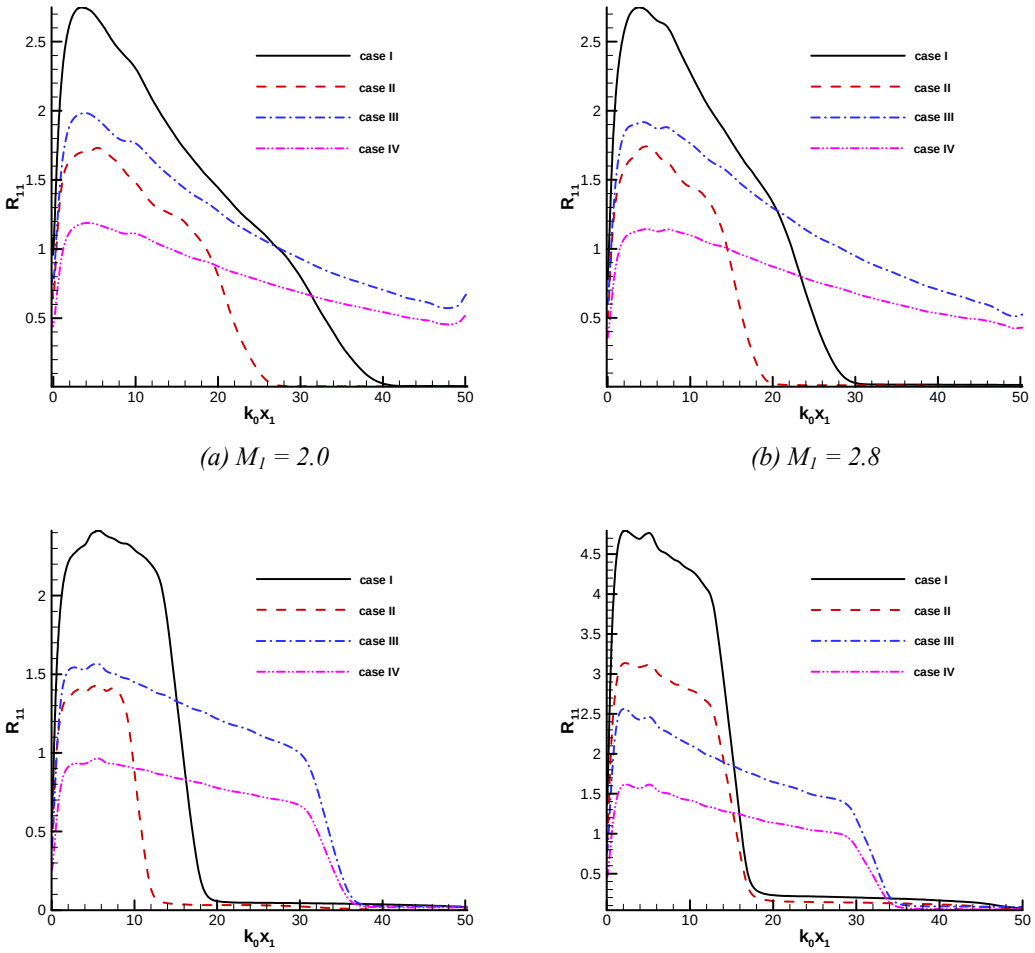

(a) M_1 = 2.0 *(b) M_1 = 2.8*

(c) M_1 = 8.8 *(d) M_1 = 30.0*

Fig. 22. Evolutions in streamwise-streamwise Reynolds stresses at a given shock Mach number.

4. Test of shock-fitting method and non-equilibrium models

The two-temperature model of air has been implemented to the fifth-order shock-fitting method with recent models of thermochemical models. Here we focus our tests on shock-fitting method and thermo-chemical models.

4.1 Gnoffo's air dissociation over 1 meter radius cylinder

Figure 23 shows the mesh and flow conditions of the test case: 5-species air over a 1-meter radius cylinder. The temperatures on the cylinder are equal to Tw (= 500 K). Catalytic boundary conditions are applied on the wall for species mass fraction. Total density is computed from pressure and translational temperature. Then species densities are calculated with total density and mass fraction. Total energy and vibration energy are calculated using species densities and two temperatures. The mass fractions of initial gas are as follows,

$$C_{N2} = 0.76 \qquad C_{O2} = 0.24 \qquad C_{NO} = C_N = C_O = 0$$

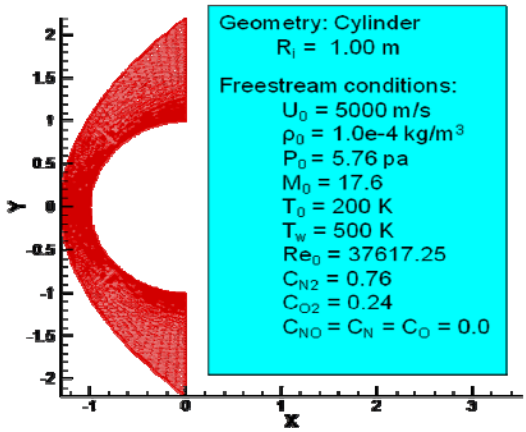

Fig. 23. Mesh sturcture and flow conditions of the test case.

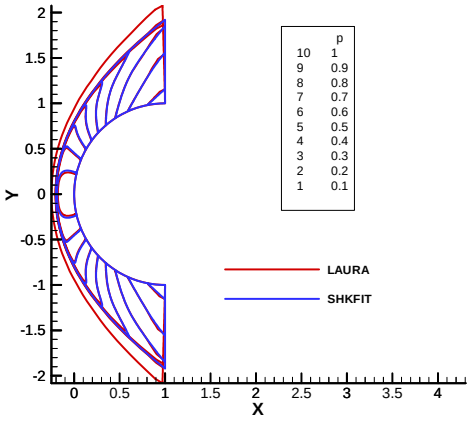

(a) Pressure

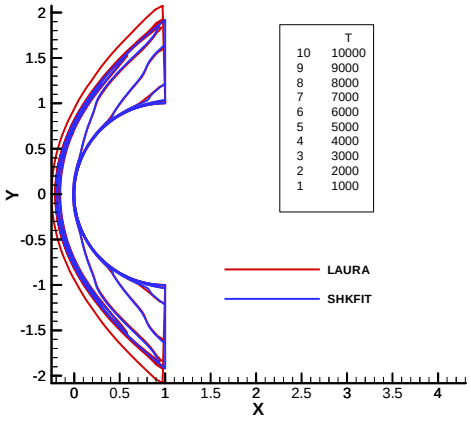

(b) Translation temperature

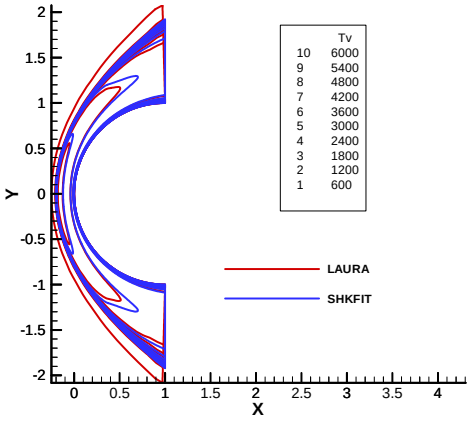

(c) Vibration temperature

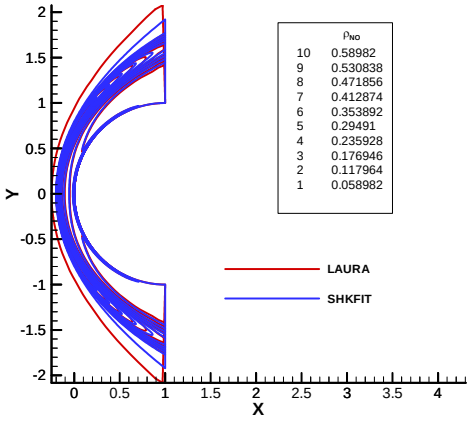

(d) Species density of NO

Fig. 24. Comparisons of flow field contours obtained from shock-fitting code with those obtained from Laura simulation.

To make the results comparable, flow conditions are exactly the same as what Gnoffo used in his simulation. The simulation results are compared with Gnoffo's results obtained from Laura. Figure 24 compares flow field contours obtained from current shock-fitting code with those obtained from Laura code. From the contours of pressure, temperatures, and NO density, it is found that shock standoff distances of the two sets of simulations have a good agreement. In addition, the flow fields near the wall have a good agreement. Near the shock, there is small discrepancy between the two sets of solution, mainly due to the different treatment of shock wave. Unlike the shock-fitting code, shock-capturing TVD scheme is applied in Laura code. Figure 24(c) shows that the vibration temperature of shock-fitting solution is significant different from that of Laura in the shock layer, which is mainly caused by the different models of vibration and electronic energy. Laura code used curved fitted vibration and electronic energy [33], whereas we used separate models for vibration energy and electronic energy.

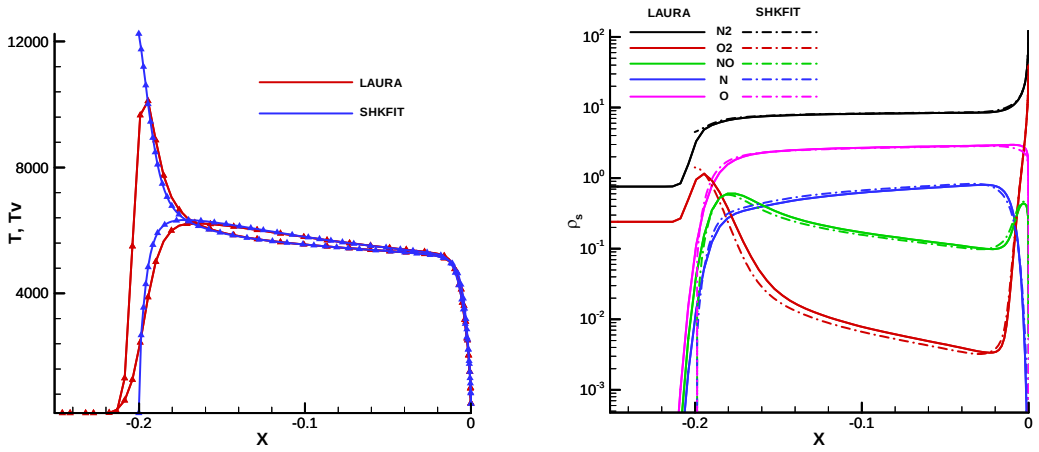

(a) Temperatures *(b) Species densities*

Fig. 25. Comparisons of flow variables along the stagnation line obtained from shock-fitting code with those obtained from Laura simulation.

Since we have detailed flow field information obtained from the Laura code, we can also compare the distributions of flow variables along the stagnation line or along the cylinder surface. For example, figure 25 compares flow variables along the stagnation line obtained from current shock-fitting code with those obtained from Laura code. These two figures also show that shock standoff distances of the two sets of simulations have a good agreement considering the different treatment of the bow shock. The distributions of temperatures and species densities along the stagnation line have a good agreement near the wall and have small discrepancy near the shock. Again, the discrepancy near the shock is due to the different treatment of shock wave. Overall, Figures 24 and 25 indicate that our shock-fitting non-equilibrium flow solver is reliable for the simulation of strong shock and turbulence interaction.

4.2 A Mach 10 flat-plate boundary layer with thermal equilibrium

The test case is got from Hudson's thesis [45]. The flow conditions of the flat-plate boundary layer are as follows,

$$M = 10 \qquad T_\infty = 278\text{K} \qquad p_\infty = 0.045\,\text{atm} \qquad u_\infty = 3351\,\text{m/s}$$

$$\rho_\infty = 0.0568\,\text{kg/m}^3 \qquad \text{Re}_\infty = 9.8425\times10^6/\text{m}$$

$$C_{N2} = 0.78 \qquad C_{O2} = 0.22 \qquad C_{NO} = C_N = C_O = 0$$

Our numerical results are compared with Hudson's theoretical solution and a recent boundary-layer solution from Prof. Tumin in Unversity of Arizona. Specifically, the temperature and velocity profiles across the boundary layer at x = 0.4 m are compared.

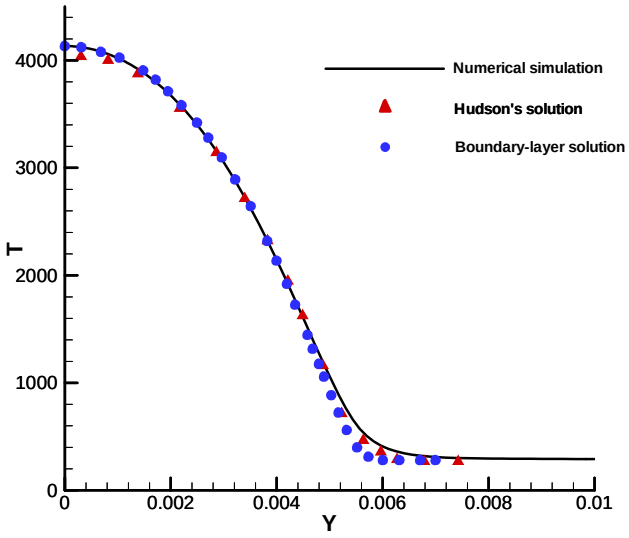

Fig. 26. Comparisons of temperature profiles across the boundary layer.

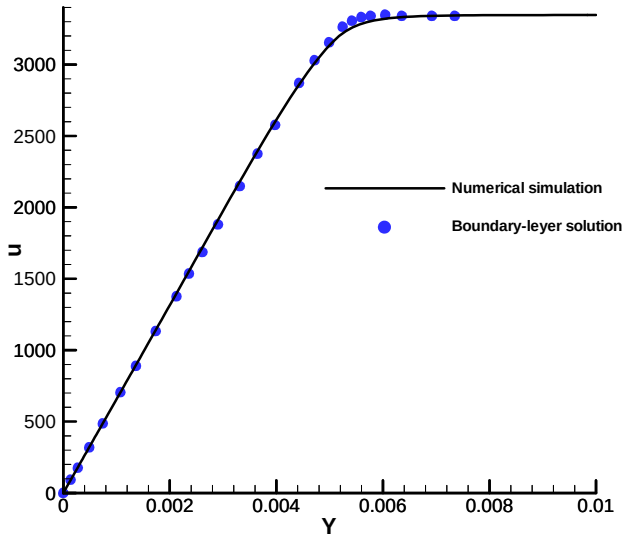

Fig. 27. Comparisons of streamwise velocity profiles across the boundary layer.

Figures 26 and 27 shows that the boundary-layer profiles obtained from our simulation have agreement with the theoretical solutions of Hudson and Tumin. The results 25 indicate that our shock-fitting non-equilibrium flow solver is reliable.

5. Summary and Future Plan

In current paper, we first conduct extensive DNS studies on the canonical strong shock and turbulence interaction problem of perfect gas flow with mean Mach numbers ranging from 2 to 30. The objectives of perfect gas flow simulations are to obtain more quantitative results and to investigate the effect of strong shock. DNS of perfect gas flow show that increasing shock-strength reduces the shock deformation. Behind the shock, mean velocity first decreases and then increases. As mean Mach number value of incoming flow is increased, the difference between laminar and post-shock turbulent mean values decreases.

The results also show that maximum values of variance of streamwise vorticity fluctuations first increase and then decrease as the shock strength is increased. The peak of streamwise vorticity fluctuations is observed for shock and turbulence interactions with Mach 2.8 shock. For stronger than Mach 2.8 shocks, there is a decrease in streamwise vorticity fluctuations. The amplification of Reynolds stress R_{11} decreases as mean Mach number is increased till 8.8, which is consistent with findings of linear interaction analysis. This trend, however, reverses as shock strength is increased beyond Mach 8.8. For stronger than Mach 8.8 shocks, Reynolds stress R_{11} is amplified as mean Mach number keeps increasing.

Since gas temperature increases dramatically after strong shocks so that numerical simulations based on perfect gas flow may not be enough. The effects of thermochemical non-equilibrium flow including internal energy excitations, translation-vibration energy relaxation, and chemical reactions among different species need to be considered. We have developed a new high-order shock-fitting solver for non-equilibrium flow simulations based on the 5-species air chemistry and recently thermal non-equilibrium models. The code package has been tested and is being applied to DNS of strong shock and turbulence interactions with thermochemical non-equilibrium effects.

Acknowledgement

The research was supported by DOE office of Science as part of a SciDAC project with “Science Application” in Turbulence and by the AFOSR/NASA National Center for Hypersonic Research in Laminar-Turbulent Transition. Numerical simulations are mainly run on TeraGrid resources provided by TACC under grant number TG-ASC100002 supported in part by the National Science Foundation. The views and conclusions contained herein are those of the authors and should not be interpreted as necessarily representing the official policies or endorsements either expressed or implied, of the Air Force Office of Scientific Research, the National Aeronautics and Space Administration, or the U.S. Government.

Reference

1. Rawat, P.S., and Zhong, X., *On high-order shock-fitting and front-tracking schemes for numerical simulation of shock–disturbance interactions.* Journal of Computational Physics, 2010. **229**(19): p. 6744-6780
2. Kovasznay, L.S.G., *Turbulence in supersonic flow.* Journal of the Aeronautical Sciences, 1953. **20**(10): p. 657-682.
3. Moore, F.K., *Unsteady oblique interaction of a shock wave with a plane disturbances.* NACA TN-2879 (Also as NACA Rep. 1165), 1953.
4. Kerrebrock, J.L., *The interaction of flow discontinuities with small disturbances in a compressible fluid.* PhD thesis, California Institute of Technology, 1956.

5. Goldstein, M.E., *Turbulence generated by the interaction of entropy fluctuations with non-uniform mean flows.* Journal of Fluid Mechanics, 1979. **93**: p. 209-224.
6. Lee, L., Moin, P., and Lele, S. K., *Interaction of isotropic turbulence with a shock wave.* Report TF-52. Dept. Mech. Eng., Stanford Univ., CA, 1992.
7. Lee, L., Lele, S. K., and Moin, P., *Direct numerical simulation of isotropic turbulence interacting with a weak shock wave.* Journal of Fluid Mechanics, 1993. **251**: p. 533-562.
8. Mahesh, K.A., Lee, L., Lele, S. K., and Moin, P., *The interaction of an isotropic field of acoustic waves with a shock wave.* Journal of Fluid Mechanics, 1995. **300**: p. 383-407.
9. Mahesh, K.A., Lele, S. K., and Moin, P., *The influence of entropy fluctuations on the interaction of turbulence with a shock wave.* Journal of Fluid Mechanics, 1997. **334**: p. 353-379.
10. Fabre, D., Jacquin, L., and Sesterhenn, J., *Linear interaction of a cylindrical entropy spot with a shock.* Journal of Physics of Fluids A, 2001. **13**(8): p. 2403-2422.
11. Pao, S.P., and Salas, M. D., *A numerical study of two-dimensional shock vortex interaction.* AIAA Paper 81-1205, 1981.
12. Zang, T.A., Hussaini, M. Y., and Bushnell, D. M. , *Numerical Computations of Turbulence Amplification in Shock-Wave Interactions.* AIAA Journal, 1984. **22**(1): p. 13-21.
13. Hussaini, M.Y., Kopriva, D., Salas, M. D., and Zang, T. A., *Spectral methods for the Euler equations. II - Chebyshev methods and shock fitting.* AIAA Journal, 1987. **23**: p. 234-240.
14. Meadows, K.R., Kumar, A., and Hussaini, M. Y., *Computational Study on the Interaction between a vortex and a shock Wave.* AIAA Journal, 1991. **29**(2): p. 174-179.
15. Meadows, K.R., and Casper, J., *Computing unsteady shock waves for aeroacoustic applications.* AIAA Paper 1993-4329, 1993.
16. Grasso, F., and Pirozzoli, S. , *Shock-wave-vortex interactions: shock and vortex deformations, and sound production.* Theoretical and Computational Fluid Dynamics, 1993. **13**(6): p. 421-456.
17. Andreopoulos, Y., Agui, J. H., and Briassulis, G., *Shock wave-turbulence interactions.* Annual Review of Fluid Mechanics 2000. **32**: p. 309-345.
18. Hannappel, R., and Friedrich, R., *Direct numerical simulation of a Mach 2 shock interacting with isotropic turbulence.* Applied Scientific Research, 1995. **54**: p. 205-221.
19. Jamme, S., Cazalbou, J. B., Torres, F., and Chassaing, P., *Direct numerical simulation of the interaction between a shock wave and various types of isotropic turbulence.* Flow, Turbulence and Combustion, 2202. **68**: p. 227-268.
20. Adams, N.A., and Shariff, K., *A high-resolution hybrid compact-ENO scheme for shock turbulence interaction problems.* Journal of Computational Physics, 1996. **127**(27): p. 57-.
21. Adams, N.A., and Shariff, K., *Direct numerical simulation of turbulent compression corner flow.* Theoretical and Computational Fluid Dynamics, 1998. **12**: p. 109-129.
22. Pirozzoli, S., *Conservative hybrid compact-WENO schemes for shock-turbulence interaction.* Journal of Computational Physics, 2002. **178**(1): p. 81-117.
23. Ducros, F., Ferrand, V., Nicoud, F.,Weber, C., Darracq, D., Gacherieu C., and Poinsot, T., *Large eddy simulation of the shock/turbulence interaction.* Journal of Computational Physics, 1999. **152**: p. 517-549.
24. Lee, S., Lele, S. K., and Moin, P., *Interaction of isotropic turbulence with shock waves: effect of shock strength.* Journal of Fluid Mechanics, 1997. **340**: p. 225-247.
25. Jamme, S., Cazalbou, J. B., Torres, F., and Chassaing, P., *Direct numerical simulation of the interaction between a shock wave and various types of isotropic turbulence.* Flow, Turbulence and Combustion, 2002. **68**: p. 227-268.
26. Lee, T.K., and Zhong, X., *Spurious numerical oscillations in simulation of supersonic flows using shock-capturing schemes.* AIAA Journal, 1999. **37**(3): p. 313-319.

27. Agui, J.H., *Shock wave interactions with turbulence and vortices*. 1998, PhD Thesis, City University of New York: New York.
28. Lele, S.K., and Larsson, J., *Shock-turbulence interaction: What we know and what we can learn from peta-scale simulations.* Journal of Physics: Conference Series, 2009. **180**(012032).
29. Rawat, P.S., and Zhong, X., *Direct Numerical Simulations of Turbulent Flow Interactions with Strong Shocks Using Shock-Fitting Method.* AIAA paper 2011-649, 2011.
30. Johnsen, E., Larsson, J., Bhagatwala, A. V., Cabot, W. H., Moin, P., Olson, B. J., Rawat, P. S., Shankar, S. K., Sjögreen, B., Yee, H. C., Zhong, X., and Lele, S. K., *Assessment of high-resolution methods for numerical simulations of compressible turbulence with shock waves.* Journal of Computational Physics, 2010. **229**(4): p. 1213-1237.
31. Vincenti, W.G., and Kruger Jr., C. H., *Introduction to Physical Gas Dynamics* 1967: Krieger Publishing Co, INC.
32. Hash, D., Olejniczak, J, Wright, M. J., Dinish, P., Pulsonetti, M., Hollis, B. R., Gnoffo, P. A., Barnhard, M., Nompelis, I., and Candler, G., *FIRE II Calculations for Hypersonic Nonequilibrium Aerothermodynamics Code Validation: DPLR, LAURA, and US3D*. 2007, AIAA 2007-0605.
33. Gnoffo, P.A., Gupta, R. N., and Shinn, J. L., *Conservation equations and physical models for hypersonic air flows in thermal and chemical nonequilibrium*. 1989, NASA Technical Paper 2867.
34. Candler, G.V., *The computation of weakly ionized hypersonic flows in thermo-chemical nonequilibrium*. 1988, Stanford University.
35. Gupta, R.N., Yos, J. M., Thompson, R. A., and Lee, K-P., *A Review of Reaction Rates and Thermodynamic and Transport Properties for an 11-Species Air Model for Chemical and Thermal Nonequilibrium Calculations to 30 000 K*. 1990, NASA Reference Publication 1232.
36. Park, C., *Nonequilibrium hypersonic aerothermodynamics*. 1990, New York: Wiley. .
37. Zhong, X., *High-order finite-difference schemes for numerical simulation of hypersonic boundary-layer transition.* Journal of Computational Physics, 1998. **144**: p. 662-709.
38. Lee, L., Lele, S. K., and Moin, P., *Simulation of spatially evolving compressible turbulence and the applicability of Taylor's Hypothesis.* Physics of Fluids A, 1992. **4**: p. 1521-1530.
39. Erlebacher, G., Hussaini, Y., Kreiss, H. O., and Sarkar, S., *The Analysis and Simulation of Compressible Turbulence.* Theoretical and Computational Fluid Dynamics, 1990. **2**: p. 73-95.
40. Samtaney, R., Pullin, D. I., and Kosovic, B., *Direct numerical simulation of decaying compressible turbulence and shocklet statistics.* Physics of Fluids, 2001. **13**(5): p. 1415-1430.
41. Ristorcelli, J.R., and Blaisedell, G. A., *Consistent initial conditions for the DNS of compressible turbulence.* Physics of Fluids, 1997. **9**(1): p. 4-6.
42. Moin, P., and Mahesh, K., *Direct Numerical Simulation: A tool in turbulence research.* Annual Review of Fluid Mechanics, 1998. **30**: p. 539-578.
43. Larsson, J., and Lele, S.K., *Direct numerical simulation of canonical shock/turbulence interaction.* Physics of Fluids, 2009. **21**(12): p. 126101-126101-12.
44. Lele, S.K., *Shock-jump relations in a turbulent flow.* Physics of Fluids, 1992. **4**: p. 2900-2905.
45. Hudson, M.L., *Linear Stability of Hypersonic Flows in Thermal and Chemical Nonequilibrium*. 1996, North Carolina State University.